The GEOVIDE cruise in May-June 2014 reveals an intense Meridional Overturning Circulation over a cold and fresh subpolar North Atlantic

Patricia Zunino[1], Pascale Lherminier[2], Herlé Mercier[1], Nathalie Daniault[3], Maribel I. García-Ibáñez [4] and Fiz F. Pérez[4]

[1] CNRS, Laboratoire d'Océanographie Physique et Spatiale (LOPS), IUEM, Plouzané, France.

[2] Ifremer, Laboratoire d'Océanographie Physique et Spatiale (LOPS), IUEM, Plouzané, France.

[3] Université de Bretagne Occidentale, Laboratoire d'Océanographie Physique et Spatiale (LOPS), IUEM, Plouzané, France.

[4] Instituto de Investigaciones Marinas, IIM-CSIC, 36208 Vigo, Spain

Corresponding author: pzuninor@ifremer.fr

Abstract

The GEOVIDE cruise was carried out in the subpolar North Atlantic (SPNA), along the OVIDE section and across the Labrador Sea, in May–June 2014. It was planned to clarify the distribution of the trace elements and their isotopes in the SPNA as part of the GEOTRACES international program. This paper focuses on the state of the circulation and distribution of thermohaline properties during the cruise. In terms of circulation, the comparison with the 2002–2012 mean state shows a more intense Irminger current and also a weaker North Atlantic Current, with a transfer of volume transport from its northern to its central branch. However, those anomalies are compatible with the variability already observed along the OVIDE section in the 2000s. In terms of properties, the surface waters of the eastern SPNA were much colder and fresher than the averages over 2002–2012. In spite of negative temperature anomalies in the surface waters, the heat transport across the OVIDE section, estimated at 0.56 ± 0.06 PW, was the largest measured since 2002. This relatively large value is related to the relatively strong Meridional Overturning Circulation measured across the OVIDE section during GEOVIDE (18.7 ± 3.0 Sv). Analyzing the air-sea heat and freshwater fluxes over the eastern SPNA in relation to the heat and freshwater content changes observed during 2013 and 2014, we concluded that, at short time-scale, these changes were mainly driven by air-sea heat and freshwater fluxes rather than by ocean circulation.

1. Introduction

The subpolar North Atlantic (SPNA) is a key area for studying the effect of climate change in the ocean. The deep convection processes there behave as a driving mechanism for the Meridional Overturning Circulation (Kuhlbrodt et al., 2007; Rhein et al., 2011; Sarafanov et al., 2012), which transports heat to high latitudes in the North Atlantic and is predicted to slow down at the end of the present century (IPCC, 2007). Additionally, the SPNA presents the highest anthropogenic CO_2 storage rate of all oceans (Khatiwala et al., 2013), due to both the advection of surface waters enriched with anthropogenic CO_2 in the subtropical North Atlantic (Pérez et al., 2013; Zunino et al., 2015) and their deep injection in the subpolar gyre (Pérez et al., 2010). In addition, the SPNA is one of the few oceanic regions where significant cooling was detected over 1955–2010 while the rest of the world oceans was warming (Levitus et al., 2012). For all these reasons, the SPNA has been the target of several projects and broadly sampled by oceanographic cruises. As part of the OVIDE project (http://www.umr-lops.fr/Projets/Projets-actifs/OVIDE), the OVIDE section has been sampled biennially in summer since 2002 to collect data related to the circulation and the carbon cycle. Its path between Greenland and Portugal is shown in Fig. 1 along with a schematic view of the upper, intermediate and deep circulations in the SPNA adapted from Daniault et al. (2016), which will be referred to as D2016 hereafter.

The international GEOTRACES program (http://www.geotraces.org/) aims to characterize the trace elements and their isotopes (TEIs) in the world ocean. These TEIs are Fe, Al, Zn, Mn, Cd, Cu, $\delta^{15}N$, $\delta^{13}C$, $^{231}Pa/^{230}Th$, Pb and Nd in the dissolved phase as well as in particles and aerosols. TEIs provide constraints and flux estimates that can be used to reconstruct the past environmental conditions. The GEOVIDE project is a French contribution to the GEOTRACES program. It is dedicated to measure the large-scale distributions of TEIs in the SPNA for the first time. The GEOVIDE cruise was carried out in May–June 2014 and was composed of two sections: one along the OVIDE line (its 7^{th} repetition) and another one crossing the Labrador Sea, from Cape Farewell (Greenland) to St John's (Canada). The expertise gained on water mass properties and circulation across the OVIDE section (García-Ibáñez et al., 2015; D2016) first helped to determine the optimal geographic distribution of the TEI sampling. However, the ocean is not steady, and the present study shows how anomalous, in terms of thermohaline properties and circulation, the eastern SPNA was in summer 2014 compared with the previous decade, and thus provides guidance for the interpretation of the measured distribution of TEIs.

The ocean has taken up 90% of the heat accumulated in the climate system since 1971 (Riser et al., 2016). In this context, it is striking to note the absence of a significant warming trend in between 50 °N and 60 °N in the Atlantic Ocean between 1955 and 2010 (Levitus et al., 2012; Sgubin et al., 2017). In fact, an important variability in the heat and freshwater content occurs in the SPNA at the decadal or longer time-scales. Since 1960, different periods of cooling (warming) or freshening (salinification) in the SPNA have been detected. Negative salinity anomalies were observed in the SPNA surface waters during the 1970s, and referred to as the Great Salinity Anomaly event. They were explained by a large pulse of freshwater getting into the SPNA through the Denmark Strait (Dickson et al. 1988; Robson et al., 2014). Concurrently, the subpolar gyre (SPG) started a cold phase that persisted up to the beginning of the 1990s. Later, from mid-1990s to mid-2000s, positive anomalies of temperature and salinity in the surface waters of the SPNA were observed, coinciding with the contraction and weakening of the SPG (e.g. Bersch, 2002; 2007; Sarafanov et al., 2008; Häkkinen et al., 2011). Many works analyzed the causes of the observed decadal to multi-decadal variability in ocean heat content in the SPNA by analysis of both observations and model outputs (e.g. Deshayes and Frankignoul, 2008; Lohmann et al., 2009; Robson et al., 2012; 2014; Barrier et al., 2015)**.** They concluded that the heat content anomalies in the SPNA at long time-scale are mainly controlled by changes in the lateral advection, linked to changes in the intensity of the Atlantic Meridional Overturning Circulation (AMOC). At shorter period of time, the air-sea flux causes significant heat and freshwater changes, by intensifying or buffering the effect of the anomalies caused by the lateral advection (Barrier et al., 2015; Desbruyères et al., 2015; Grist et al., 2015).

Recently, Hermanson et al. (2014) and Robson et al. (2016; 2017), analyzed outputs of coupled climate models, and identified a new cooling and freshening period from the mid-2000s. Their results coincide with observations: Johnson et al. (2016) documented a SPNA region cooler in 2014 than in 1993-2014 climatology, this cooling intensified in 2015 and 2016 (Yashayaev and Loder, 2016; 2017). Over the eastern SPNA, Grist et al. (2015) analyzed the winter 2014 anomalous air-sea fluxes and their imprint on the ocean. Based on EN4 ocean reanalysis, they detected negative temperature anomalies in the surface waters, which they related to anomalous air-sea heat fluxes. Conversely, Holliday et al. (2015), who found evidence of similar cooling and also of freshening in the Iceland basins from 2010–2011 to 2014, privileged the hypothesis of a remote source of those anomalies, writing that

96 **"**the eastern SPNA is once again being influenced by cold, fresh western subpolar water". We
97 will discuss both hypotheses in this study.

98 In this article, we first contextualize the physical background of the GEOVIDE cruise to help
99 for the interpretation of distribution of TEIs in the eastern SPNA. The works dealing with
100 TEIs distribution will be published in this Biogeoscience GEOVIDE special issue: Cossa et
101 al. (2017), Lemaître et al. (2017), García-Ibáñez et al., (2017), and other manuscripts are in
102 preparation. Subsequently, by the analysis of the GEOVIDE cruise data along with altimetry,
103 oceanic database and air-sea flux data, we disentangle the causes of the anomalous
104 thermohaline properties of the surface and intermediate layers of the eastern SPNA in May–
105 June 2014. The paper is organized as follows. Data and methodology are described in section
106 2. Section 3 displays the main results on the large and mesoscale patterns of the circulation
107 and thermohaline anomalies in 2014, settling the GEOVIDE TEIs stations in this context.
108 These results are discussed in section 4. Finally, section 5 presents the main conclusions.

109

110 **2. Data and Methods**

111 **2.1. GEOVIDE data**

112 The GEOVIDE cruise was the French contribution to the GEOTRACES program
113 (http://www.geotraces.org/) in the North Atlantic. It was carried out on board the French R/V
114 *Pourquoi Pas*? from 15 May 2014 to 30 June 2014. A total of 78 stations were measured and
115 sampled along two hydrographic sections: i) the 7th repetition of the OVIDE section (from
116 Portugal to Greenland) and ii) a section across the southern Labrador Sea, between Cape
117 Farewell and Newfoundland. In this paper we only deal with data from the OVIDE section.
118 Because this cruise was inserted in the GEOTRACES project, a large number of parameters
119 were measured, some of them present in the ocean in very low concentration. Therefore,
120 several rosette casts (up to 9) had to be done at some stations; the full-depth cast with salinity
121 and oxygen samples was always used as reference for physical characterization of water
122 masses and currents. Stations were named according to the parameters to be measured and the
123 different number of casts to be carried out: Short, Large, XLarge and Super stations. Nearly
124 all the TEIs required by the GEOTRACES program were sampled at Xlarge and Super
125 stations, which positions were selected to be representative of the different hydrographic
126 regions, as detailed in section 3.4. Because the ship time was limited to 45 days, the number

of stations along the OVIDE section was reduced compared with previous cruises, with 60 stations within 6 weeks during GEOVIDE compared with 95 stations usually sampled within about 3 weeks in previous OVIDE cruises.

Conductivity, temperature, pressure and dissolved oxygen were measured using a CTD SBE911 equipped with an SBE-43. The rosette was also equipped with 22 bottles for collecting seawater. For calibration purposes, salinity and oxygen were determined on board from seawater samples, using a salinometer and titration, respectively. The final accuracy was 0.001 °C, 0.002, and 2 µmol kg^{-1} for temperature, salinity and oxygen, respectively. Figure 2 shows the calibrated temperature, salinity and oxygen measured during CTD-O_2 down casts of the OVIDE section. For more details about the water mass properties and their distributions along the OVIDE section between 2002 and 2012, see García-Ibáñez et al. (2015) and D2016.

Finally, the velocities of the upper waters were measured continuously with two ship-mounted ADCP (Ocean Surveyors) at a frequency of 38 Hz and 150 Hz, measuring down to 1000 m and 300 m with vertical resolutions of 24 m and 8 m, respectively.

The winter mixed layer depth (WMLD) was estimated along the OVIDE section by visual inspection of the individual potential density and Apparent Oxygen Utilization (AOU) profiles measured during the GEOVIDE cruise. Because the cruise was conducted in summer, the seasonal mixed layer was disregarded and the WMLD was defined as the depth where the slope of the density profile accentuated and the AOU was larger than 0.6 µmol kg^{-1}. The latter value was chosen because it was the best fit with the density criteria at most stations.

2.2. Inverse model

The absolute geostrophic field orthogonal to the section was estimated by a box inverse model using the hydrographic profiles measured at each station, current measured by the ship ADCP (S-ADCP) and a volume conservation constraint of 1 Sv northward (Lherminier et al., 2007). For inversion constrain, the S-ADCP data were averaged between stations in layers where the shear of the velocity profile was consistent with geostrophic velocity profiles. The inverse model is based on the thermal wind equation and the least-squares formalism following the method described in Mercier et al. (1986) and Lux et al. (2001). Additionally, the Ekman velocities were added to the inverse model: the Ekman transport was estimated from NCEP winds (Kalnay et al., 1996) and equally distributed over the first 30 m. The velocity errors were given by the resulting covariance matrix from the box inverse model. For more details about the inverse model configuration specific to OVIDE, see Lherminier et al. (2007, 2010) and Gourcuff et al. (2011). The volume transports were computed by multiplying velocities

by the distances between two stations. Their errors were obtained from the full covariance matrix of velocities, taking into account error correlations, as explained in Mercier (1986).

For the computation of transport across the OVIDE section from GEOVIDE data, the first challenge was to determine the proper spatial sub-sampling. In order to select the station positions and minimize the error associated with the sub-sampling, a sensitivity analysis was performed with the data from the 2010 OVIDE cruise before the GEOVIDE cruise was carried out. The chosen compromise was efficient to represent all the main water masses and gave similar AMOC amplitude and consistent transports of the currents crossing the section, although the errors on the 2010 regional features increased when subsampled. However, in 2014, we used a more precise S-ADCP, reducing the S-ADCP error contribution to the inverse model solution. Consequently, the final errors of the dynamical structures in 2014 are of the same order of magnitude than the errors estimated in previous OVIDE cruises.

The velocities measured by the S-ADCP and those resulting from the inverse model are compared in Fig. 3 (note that the vertical scale differs between the subplots). We see that the inverse model results reproduce the main features of the large-scale circulation captured by the S-ADCP. As expected, mesoscale and ageostrophic structures of horizontal sizes smaller than the distances between stations are visible on the S-ADCP section but are not resolved in the inverse model solution (e.g. between stations 45 and 38 or between stations 32 and 27). However, because the geostrophic velocity is an average between stations, this does not imply any bias in the transports. This outcome is also supported by Gourcuff et al. (2011) who, comparing altimetry and S-ADCP data, showed that the contributions of ageostrophic motions tend to cancel out when averaged over the distance between stations.

The inverse model estimates the absolute geostrophic transport and the transport of heat and other tracers. The under-sampling of the GEOVIDE cruise notably increases the errors associated with the transport of tracers, because the horizontal gradients of those tracers are less well resolved. The tracer considered in this work is temperature. By applying the GEOVIDE sub-sampling to the inversion of the OVIDE 2010 data, we estimated a supplementary and independent sampling error of 0.04 PW for heat transport.

2.3. Oceanic database

We used the In Situ Analysis System (ISAS) analysis (Gaillard et al., 2016), which, based on Argo profiles and other qualified *in situ* observations (cruises, fixed-point time series, ships of opportunity, etc.), produced monthly gridded fields of temperature and salinity profiles by

optimal interpolation for the period since 2002. We also used EN4 reanalysis. Similar to ISAS, EN4 reanalysis is an optimal interpolation that incorporates *in situ* data measured since 1900, filling gaps by extrapolation from the observational data using covariances from the Hadley Centre model (Good et al., 2013). We also used the temperature and salinity analysis developed by JAMSTEC (Hosoda et al., 2008), which is also an optimal interpolation based on Argo profiles, Triangle Trans-Ocean Buoy Network (TRITON) and other *in situ* observations.

First, we evaluated the temporal and horizontal extension of the potential temperature (θ) and salinity (S) anomalies detected in the surface layer from ISAS: both properties were averaged between 20 and 500 m at each ISAS grid point in the North Atlantic, and monthly anomalies were then estimated with respect to the 2002–2012 mean values. Second, ISAS, EN4 and JAMSTEC databases were used to evaluate the heat and freshwater content changes in the upper 1000 m in the region delimited by 40–60 °N and 45–10 °W: for each month the heat content (HC_{month}) and the freshwater content (FWC_{month}) of the volume of water in the box previously defined was estimated following eq. 1 and eq. 2, respectively:

$$HC_{month} = \sum_{z=1}^{z=n} \sum_{i=1}^{i=n} \theta_{z,i} * Cp_{z,i} * \rho_{z,i} * V_{z,i} \qquad \text{eq. 1}$$

$$FWC_{month} = \sum_{z=1}^{z=n} \sum_{i=1}^{i=n} \frac{(35 - S_{z,i}) * V_{z,i}}{35} \qquad \text{eq. 2}$$

where z and i are the depth levels and grid points of the database, and $Cp_{z,i}$, $\rho_{z,i}$ and $V_{z,i}$ are the heat content capacity, density and volume of each depth level and grid point of the database.

2.4. Air-sea flux data

In order to evaluate the role of atmospheric forcing on the θ and S anomalies observed during the GEOVIDE cruise, re-analyzed ERA-Interim data (Berrisford et al., 2011) and NCEP data (Kanamitsu et al., 2002, http://www.esrl.noaa.gov/psd/) were processed. In particular, we estimated seasonal anomalies of net air-sea heat flux (and its components: sensible heat, latent heat, net longwave radiation and net shortwave radiation) and freshwater flux (and its components: precipitation and evaporation) as follows. Firstly, seasonal means were computed defining winter as DJF, spring as MAM, summer as JJA and autumn as SON. Secondly, seasonal anomalies were calculated relative to the mean seasonal cycle of 2002–2012. Finally, the anomalies of winter–spring 2014 that preceded the GEOVIDE cruise were estimated.

Furthermore, the monthly time series of net air-sea heat and freshwater fluxes were used to evaluate the contribution of the atmospheric forcing to the observed heat and freshwater content changes in the box defined in section 2.3. Specifically, we integrated net air-sea heat and freshwater fluxes**,** given every 12h/6h in ERA-INTERIM/NCEP, from January 16, 2013 to December 15, 2014. The resulting time series were compared with the monthly time series of heat/freshwater content change between one month and the previous month, accumulated from January 2013 to December 2014.

3. Results

3.1. Circulation across the OVIDE section in 2014

The OVIDE section is intersected by permanent currents and gyres that are described by D2016 using the average measurements from the first 6 OVIDE cruises (2002 – 2012). This section presents the intensity, location and extension of these dynamical structures during the GEOVIDE cruise. The results showed hereafter are based on the solution of the inverse model (see Fig. 3b). Despite the mesoscale structures typical of a single occupation of the section, we can identify and quantify all the main patterns described by D2016.

Near Greenland, the water flowing southwestward guided by the continental slope is the Western Boundary Current (WBC): it has two components, the East Greenland-Irminger Current (EGIC σ_0 < 27.8 kg m^{-3}) and the Deep Western Boundary Current (DWBC, σ_0 > 27.8 kg m^{-3}). During the GEOVIDE cruise, the extension of the DWBC towards the central Irminger Sea at depths > 2000 m (see Fig. 3b) is marked by a bottom mesoscale feature typical of the plume structure of the overflow (Spall and Price, 1997). The total intensity of the WBC was estimated at 30.3 ± 2.1 Sv southward.

The cyclonic gyre defined as the Irminger Gyre (IG) by Väge et al. (2011) can be seen in the western part of the central Irminger Sea. Following their definition, we quantified the intensity of the IG by integrating the northward transport above the isotach 0 m s^{-1} (Fig. 3b), which amounted to 6.8 ± 3.0 Sv.

The Irminger Current (IC) flows northeastwards along the western flank of the Reykjanes Ridge. In 2014, its top to bottom integrated transport amounted to 17.5 ± 7.3 Sv, which

accounts for both, the northward and the southward currents east of the IG. Considering only the northward velocities brings the IC intensity to a value of 22.7 ± 6.5 Sv.

The Eastern Reykjanes Ridge Current (ERRC) flows southwestward east of the Reykjanes Ridge. In 2014, its top-to-bottom integrated transport, between the Reykjanes Ridge and station 34 (Fig. 3), amounted to 13.6 ± 6.0 Sv southward.

The North Atlantic Current (NAC) at the OVIDE section consists of meandering branches flowing northeastward between the center of the Iceland Basin and the Azores-Biscay Rise (D2016). To determine its horizontal extension, we used the top-to-bottom volume transport accumulated from Greenland to each GEOVIDE station (the barotropic stream function**,** Fig. 4) and the AVISO altimetry data (Fig. 5). The NAC intensity was quantified as the accumulated transport from the relative minimum of the barotropic stream function in the central Iceland Basin up to the maximum of the barotropic stream function in the Western European Basin (D2016). In the Iceland Basin, we found two relative minima of the stream function (Fig. 4) due to the presence of an anticyclonic eddy, which was considered as part of the NAC, as justified in the next section. The limits of the NAC along the OVIDE section are indicated by white circles in Fig. 5, between which the different branches of the NAC appear as energetic northeastward currents. The top to bottom intensity of the NAC in 2014 amounted to 32.2 ± 11.4 Sv. Following D2016, three different branches of the NAC can be differentiated: the northern branch (NNAC), the subarctic front (SAF) and the southern branch (SNAC). The SAF is identified as the concomitant intense northward transport and salinity increase around 22.5 °W (Fig. 4). In 2014, top-to-bottom transport of the different NAC branches was -0.1 ± 6.4 Sv, 25.0 ± 3.0 Sv and 7.3 ± 4.9 Sv, respectively. Note that the net transport in the northern branch is quasi null with a large associated error and, by contrast, the SAF bears a very intense central branch. This point is discussed in section 4.

The easternmost dynamical feature of the OVIDE section is the NAC recirculation. Its intensity of 10.1 ± 6.4 Sv southwestward is determined as the top-to-bottom accumulated transport between the southern limit of the NAC and the easternmost station of the OVIDE section.

The intensity of the AMOC across the OVIDE section**,** referred as MOC hereafter**,** was defined from the velocities given by the inverse model as the maximum of the surface to bottom integrated stream function computed in vertical coordinates of potential density referenced to 1000 m (σ_1). During the GEOVIDE cruise, it amounted to 18.7 ± 2.7 Sv and

was found at σ_1 = 32.15 kg m^{-3}. Additionally, using the independent monthly MOC index created by Mercier et al. (2015), which is based on altimetry and Argo data, the intensity of the MOC across the OVIDE section amounted to the compatible value of 21.3 ± 1.5 Sv in June 2014, while the 2014 annual mean value of the MOC index was 18.2 Sv.

Heat transport during the GEOVIDE cruise was estimated at 0.56 ± 0.06 PW. Following the Bryden and Imawaki (2001) methodology adapted by Mercier et al. (2015) in isopycnal coordinates (see their equation 1), we found 0.50 PW transported by the overturning circulation, 0.04 PW by the horizontal or gyre circulation and 0.02 PW by the net transport across the section.

3.2. Fronts and eddies

Together with the above-mentioned permanent circulation features, we observed some remarkable eddies during the GEOVIDE cruise that could modify the "typical" patterns of properties defined by D2016 or García-Ibáñez et al. (2015), and they can affect the distribution of tracers measured during the GEOVIDE cruise.

The identification of eddies and fronts was based on the analysis of surface velocities provided by AVISO (see Fig. 5), the velocity profiles given by both the S-ADCP and the inverse model (Fig. 3) and the vertical distribution of properties (Fig. 2). In Fig. 5, we identify clearly that the most energetic currents crossing the OVIDE section are the WBC, close to Greenland, and the NAC with its different branches. Moreover, all the energetic eddies intersecting the OVIDE section were observed in the NAC (Fig. 6) and identified on Fig. 3. From north to south, the first eddy intersecting the section, referred to as the northern eddy, is detected at 56.5° N, 27° W (Fig. 5). This eddy lies between stations 34 and 32 (Fig. 3; Fig. 6), extending from the surface to the bottom but intensified in the upper 600 m. From Fig. 6, we inferred that this eddy was generated in April at approximately 56.5 °N, 26 °W from the meandering of the NAC north of the OVIDE section; its position is marked by yellow squares in Fig. 6. In May 2014, the eddy was totally formed and intersected the section between 55.5° N and 57° N. In June 2014, the eddy moved southwestward, in agreement with the general displacement of anticyclonic eddies in the SPNA. The core of the northern eddy, between stations 34 and 32 in Figs. 2a and 2b, shows properties warmer and saltier than the surrounding water, confirming the NAC origin of this eddy; this is why this anticyclonic eddy has been considered as part of the northern branch of the NAC. Note that in May–June, the

net transport of this eddy**,** from surface to the bottom, is almost 0 Sv (see Fig. 4 between stations 34 and 32).

A large anticyclonic eddy, the central eddy, is observed at 53 °N, 26 °W, at a tangent to the OVIDE section between stations 30 and 29 (red squares in Fig. 6). However, no signal was detected in the barotropic stream function (Fig. 4) since the northward and southward velocities (Fig. 3a) compensated once integrated between the two stations (Fig. 3b). It is noteworthy that, contrary to the previous anticyclonic eddy, this one is stationary south of the OVIDE section between March and June (Fig. 6) and was found to be quasi-permanent in the altimetry data since 1993 (figure not shown). Hydrographic properties measured at stations 29 and 30 showed cold and fresh water between 350 m and 500 m depth, typical of the Subarctic Intermediate Water (SAIW), which is most likely **trapped** by this anticyclonic eddy.

The most remarkable front present on the OVIDE section is the SAF, associated with the central branch of the NAC. Along the OVIDE section, it is situated between 49.5 °N and 51°N in latitude and 23.5 °W and 22 °W in longitude (red points in Fig. 5 and 6). This front separates cold and fresh water of subpolar origin from warm and salty water of subtropical origin; it is identifiable in Fig. 2 at station 26 by the steep slope of the isotherms and isohalines. The position of this front is known to vary spatially (Bersch 2002; Bower and Von Appen, 2008; Lherminier et al., 2010), creating anomalies of salinity and temperature that will be discussed later.

Finally, also in Fig. 5, we identified the southern branch of the NAC with a maximum in the eastward velocities found at 46.5 °N, 22 °W, west of GEOVIDE superstation 21. Despite a very rich mesoscale activity we can distinguish in Fig. 5 that the southern NAC splits into two sub-branches before crossing the OVIDE section, in agreement with D2016. The northernmost sub-branch cuts the section between stations 23 and 24 at 48.5 °N, 21 °W. The southernmost sub-branch evolves into a cyclonic eddy (the southern cyclonic eddy**,** light green square in Fig. 6) that intersects the OVIDE section south of station 21. This eddy is also observed in the velocity profiles (Fig. 3) between stations 21 and 19, as well as by the uplifting of isotherms and isohalines in Fig. 2. To its southeast, an anticyclonic eddy (orange square in Fig. 6), centered on station 18, marks the southern limit of the NAC and the beginning of the southwestward recirculation. On the OVIDE section, the southern anticyclonic eddy also marks the northwest limit of the presence of Mediterranean Water at about 1000 m depth (Fig. 2b), consistently with its slow westward advection since March

(Fig. 6). Note that while the southern anticyclonic eddy (orange square in Fig. 6) looks stable over time, the southern cyclonic eddy (light green square in Fig. 6) seems more transitory since it is not clearly visible in April.

3.3. Thermohaline anomalies in 2014

The anomalies of potential temperature (θ), salinity (S) and dissolved oxygen along the OVIDE section in 2014 were computed on pressure levels (Fig. 7), with respect to the average of the six repetitions of the OVIDE section (summers 2002, 2004, 2006, 2008, 2010 and 2012). Only anomalies larger than one standard deviation from the mean are represented in Fig. 7. In the following, S and θ anomalies were quantified as the mean values of the anomaly patches represented in Fig. 7. We identified 4 different types of anomalies along the OVIDE section. First, negative anomalies in surface-intermediate waters were observed above the WMLD over the Reykjanes Ridge (in the IC and the ERRC) and east of 20° W (in the SNAC and its recirculation). In the former, the S and θ anomalies were quantified at -0.08 and -1.04 °C, respectively. In the latter, the negative anomalies of S and θ amounted to -0.11 and -0.70° C. In the ERRC, negative S and θ anomalies also appeared below the WMLD amounting to -0.06 and -0.80 °C, respectively. It concerns a water mass that is different from the one in the WMLD; both water masses are separated by a negative anomaly of oxygen (Fig. 2c) and a maximum of potential vorticity (not shown). The cooling and freshening of the surface-intermediate waters were not compensated in density: the cooling dominated and the water was significantly denser (Fig. not shown). Concurrently, a positive oxygen anomaly was observed.

In both the Irminger Sea and the Iceland Basin, positive anomalies of S and θ were observed in waters deeper than 1000 m. In the Irminger Sea, the S and θ anomalies amounted to 0.017 and 0.122 °C, respectively. In the Iceland Basin, they reached similar values, i.e. 0.014 and 0.125 °C. In both basins, these anomalies coincided with significant negative oxygen anomalies up to -20 µmol kg^{-1}, suggesting that this water mass was not recently ventilated.

In the Iberian Abyssal Plain (IAP), negative anomalies of S (-0.12) and θ (-0.67 °C) were observed at the level of the Mediterranean Water (MW), above and below the isopycnal 32.15 kg m^{-3}. Although remarkable, those anomalies are difficult to interpret because of the high variability of the Meddy distribution in this area.

The displacement of fronts or eddies already identified in the previous section generated other occasional anomalies. The salty and warm anomaly found at 27.4 °W, above isopycnal 32.15 kg m^{-3}, is explained by the anticyclonic eddy (the northern eddy), which advected water from the NAC. The fresh and cold anomaly localized at 25 °W is a consequence of the SAIW brought by the anticyclonic eddy (the central eddy) located at 53 °N, 26 °W and touching the OVIDE section between stations 30 and 29. Finally, the southeastward displacement of the SAF created a fresh and cold anomaly between 23 °W and 22 °W because warm and salty North Atlantic Central Water (NACW) usually found in this area was replaced by subpolar water.

In Fig. 7c, we found an increase in the ventilation in the first 1000 m, while the deeper waters are less oxygenated when compared to the 2002–2012 period. The anti-correlation between the oxygen anomalies and the θ–S anomalies will be discussed in section 4.2.

3.4. Settling the special GEOVIDE stations in the framework of the large-scale and mesoscale circulation

As part of the GEOTRACE program, seven superstations and three XLarge stations were carried out along the OVIDE section in 2014 for sampling TEIs in the SPNA. The TEIs results will be published in this Biogeoscience GEOVIDE Special Issue (e.g. Cossa et al., 2017, about mercury; Lemaître et al., 2017, about particulate barium; Le Roy et al., in prep., about radium 226; Tonnard et al., in prep., about dissolved iron). In order to facilitate the interpretation of the TEIs distribution, here, we contextualize the superstations and Xlarge stations (red and green numbers, respectively, in Figs. 2, 3 and 4, and pink stars in Fig. 5) in the physical framework described above. Apart from station 26, which was specifically selected in real-time in the middle of the SAF, and station 38 over the Reykjanes Ridge, all the other special stations are representative of relatively large hydrographic domains since they are not strongly affected by the peculiar mesoscale features described in section 3.2.

Specifically, from Greenland to Portugal, these stations were located in: the East Greenland Coastal Current (EGCC, station 53), the East Greenland-Irminger Current (EGIC, station 60, same position than 51), the Irminger Gyre (station 44, same position than station 46), in the middle of the Iceland Basin (being part of the NNAC, station 32), in the SNAC (station 21), in the center of the southward recirculation in the IAP (station 13), on the Iberian Peninsula slope (station 8) and, finally, on the Portuguese continental shelf (station 2). Importantly for the GEOTRACES community, although the superstations and XLarge stations are

representative in terms of circulation, the large-scale S–θ anomalies detailed in section 3.4 need to be taken into account when comparing GEOVIDE data with data from the previous decade.

4. Discussion

4.1. State of the circulation during the GEOVIDE cruise with respect to the mean state

We will first discuss the circulation patterns seen during the GEOVIDE cruise in comparison with the mean position, extension and intensity of the main currents intersecting the OVIDE section defined by D2016. Despite the coarse resolution of the GEOVIDE stations, all the circulation structures are identified in the inverse model solution (Table 1). The intensity of the WBC and the IG are similar to the mean state with a quite high reliability (low relative error). The transports of the ERRC and the southwestward recirculation in the IAP are also very similar to the mean state, but remained to a large degree uncertain. Conversely, the IC and NAC are different from the mean state, but not significantly.

When defining the IC as in D2016, we saw an increase in the IC intensity in 2014, but within the observed variability (Table 1). However, the such-defined IC encompasses a warm and salty northward transport and a cold and fresh southward transport. So, to go further in the analysis of IC, we compared its northward component near Reykjanes Ridge with its equivalent from the 2002–2012 mean data (not shown in D2016). In this case, the IC amounted to 22.7 ± 6.5 Sv, which is significantly larger than the northward IC computed from D2016 data: 11.0 ± 3.4 Sv. Our result is similar to the estimate of Väge et al. (2011) who quantified the IC at 19 ± 3 Sv (1991–2008). Therefore, we conclude that the thus-defined IC was strengthened in 2014 with respect to the 2002–2012 mean value. Note that the northward component of the IC, between stations 38 and 41, transports water masses that are warmer and saltier than those advected southward, between stations 41 and 45, (Fig. 2); so, the intensification of the Irminger Current is meaningful in terms of transport of warm and salty water to the north, and actually contributes to the upper limb of the MOC (Fig. 4, dotted line).

Concerning the NAC, its 2014 intensity, 32.2 ± 11.4 Sv, is weaker although within the limits of the observed variability (41.8 ± 3.7 Sv). By the decomposition of this wide current, it is very likely that the difference comes from the change in the intensity of the northern branch of the NAC: -0.1 ± 6.4 Sv was computed in GEOVIDE, while 11.0 ± 3.0 Sv was estimated by

D2016. However, the weakening of the northern branch of the NAC in 2014 was partially compensated by the doubling of transport of the NAC central branch, when compared with the 2002–2012 mean (25 ± 3 Sv vs. 14 ± 6 Sv), suggesting there was a partial transfer of transport from the northern to the central branch of the NAC.

The SAF, that bears the central branch of the NAC, shows also a remarkable southeastward displacement in 2014 with respect to the mean circulation pattern (station 26 in Fig. 1), of about 100 km. A careful study of the ADT streamlines (Fig. 8) showed that this displacement was not due to a peculiar meandering of the front and that the SAF was actually narrower and located more to the southeast in 2014, when compared to the 2002–2012 mean. Bersch et al. (2007) linked the northwestward displacement of the SAF in the eastern North Atlantic in the late 1990's to a shift from positive to negative values in the index of the North Atlantic Oscillation (NAO), which is the dominant mode of atmospheric variability over the North Atlantic. After a decade of neutral values, the winter NAO index turned positive in 2011 and continued positive in 2013 and 2014 (Hurrell et al., 2017). The southeastward displacement of the SAF is thus symmetric to Bersch et al. (2007) and consistent with their observations.

Along the OVIDE section, some permanent circulation features were observed by D2016, where the velocity was found to be in the same direction for all repeated measures over the 2002–2012 period (see their Fig. 4). In our Fig. 3, we found most of these permanent circulation features: the WBC, IC, ERRC, two deep southward veins transporting the Iceland-Scotland Overflow Water (ISOW) in the Iceland Basin, and the northward transport over Eriador Seamount in the intermediate layer. Only the "permanent" anticyclonic eddy marking the southern limit of the NAC moved: it was expected between station 20 and 21 according to the mean circulation (Fig. 1), but was instead found at station 18, i.e. more to the southeast, during the GEOVIDE cruise (and called the southern anticyclonic eddy previously).

The inverse model solution also provides a robust estimate of both the intensity of the MOC and the heat transport. We observed a heat transport of 0.56 ± 0.06 PW. To compare it with the 2002–2010 average, we used the data of Mercier et al. (2015), without data from 1997, because it did not belong to our reference period, and obtained 0.47 ± 0.05 PW. Even if the 2014 value is not statistically different from the mean, it is surprising to find such a high heat transport considering the cold anomaly observed in the NAC surface waters (Fig. 7). To determine the role of the MOC in this result, we first looked at the 2014 MOC (18.7 ± 2.7 Sv), which is 2.5 Sv higher than the 2002–2010 average (16.2 ± 2.4 Sv). Note that including 2012

data (15 Sv and 0.39 PW, not published) in the mean increases the difference with 2014. This result is in line with the observation of Rossby et al. (2017), who found that the MOC intensity at 59.5 °N was larger for the period from late-2012 to early-2016 than the average over 1993–2016. To improve our quantification of the influence of the MOC on heat transport, we used the heat transport proxy HF* built by Mercier et al. (2015), which evaluates the heat transport only driven by the diapycnal circulation, known to be the dominant term of heat transport for all the OVIDE cruises. The proxy (eq. 3) is based on the MOC intensity (MOC_σ) and the temperature difference between the upper and lower limbs of the MOC (ΔT):

$$HT^* = \rho . c_p . \Delta T . MOC_\sigma \qquad \text{(eq. 3)}$$

where HT*, ρ and c_p are the heat transport proxy, the *in situ* density and the specific heat capacity, respectively. During GEOVIDE, HT* amounted to 0.49 PW, with MOC_σ = 18.7 Sv and ΔT = 6.40 °C. The 2002–2010 mean values of HT*, MOC_σ and ΔT were 0.43 PW, 16.2 Sv and 6.79 °C, respectively. So, the heat transport index and MOC_σ were larger in 2014 than the mean values, while the ΔT was smaller, which is consistent with the cold anomaly. These results show that the larger MOC_σ measured during GEOVIDE was enough to compensate for the heat transport decrease due to the cooling of the surface waters. This result might be the effect of a short-term variability since it contrasts with the study of Desbruyères et al. (2015), who argued that the long-term variability of the ocean heat transport at the OVIDE section is dominated by the advection by the mean velocity field of temperature anomalies formed upstream rather than the velocity anomalies acting on temperature.

4.2. Negative anomalies of θ and S in surface-intermediate layers explained by the local atmospheric forcing.

The long-term evolution of heat content anomaly with respect to the 2002–2012 mean (Fig. 9) was calculated in the upper 1000m over the SPNA region delimited by 40–60 °N latitude and 45–10 °W longitude (green square in Fig. 11). As shown by Robson et al. (2016), the SPNA started a new long-term cooling period since the mid-2000s. By analyzing outputs of coupled climate models, Robson et al. (2017) argued that this new cooling period is led by the reduced ocean heat transport convergence resulting from a long term slow-down of the AMOC. Within this long-term cooling period, we will focus hereafter on the pronounced heat content drop that happened between 2013 and 2014**.**

The negative anomalies of θ and S in the surface-intermediate layers along the OVIDE section in May–June 2014 with respect to the mean 2002–2012 were actually present over the whole of the year 2014 and the whole SPNA (Fig. 10). θ and S anomalies in the ocean can be caused by changes in the lateral advection of water masses with different properties, and/or by anomalous net air-sea fluxes. Considering the high ocean heat transport observed during GEOVIDE, we analyzed the air-sea flux anomalies. The mean winter–spring (W-S 2014) anomalies of air-sea heat flux presented strong negative anomalies over the whole SPNA (Fig. 11a), i.e. the ocean lost more heat than the 2002–2012 average, with contribution of both sensible and latent air-sea heat fluxes (Fig. 11b and 11c). The spatial repartition of the freshwater budget is mainly driven by the patterns of the precipitation anomalies, with a net freshwater loss southwest of the region and a clear gain in the eastern side**.** When the net freshwater flux was integrated over our region (Fig. 12), the net freshwater gain (Fig. 11d) shows that high precipitation rates (Fig. 11f) overcame the freshwater loss by evaporation (Fig. 11e). These anomalous air-sea heat and freshwater fluxes in the eastern SPNA suggest that the negative θ and S anomalies observed in the surface-intermediate waters during GEOVIDE were mainly formed locally by atmospheric forcing.

The heat/freshwater content changes in the upper 1000 m of the ocean during the 2013–2014 period were evaluated together with the air-sea heat/freshwater fluxes in the region delimited by 40–60 °N latitude and 45–10 °W longitude. In agreement with Grist et al. (2015), we found that the air-sea heat flux is responsible for most of the cooling observed in the surface-intermediate layers. Exactly, we estimated the accumulated air-sea heat loss from summer 2013 to summer 2014 at 6.8 10^{21} J, while the accumulated ocean heat loss for the same period amounted to 4.8 10^{21} J (averaged of ISAS, EN4 and JAMSTEC estimates). This result is also in agreement with the findings of Duchez et al. (2016), who argued the 2013–2015 intense air-sea heat fluxes drove water masses transformation, which is an irreversible process. Recently, Frajka-Williams et al. (2017) explained that such short-term cooling is mainly caused by the atmospheric forcing since the hypothetical slow-down of the AMOC would take longer to generate a cooling of this magnitude. Concerning the freshwater, we detected that, despite the variability in freshwater content change at intra-seasonal and seasonal time-scales (Fig. 12), there is a good agreement between the trends shown by the ocean freshwater content and the air-sea freshwater flux over the 2013–2014 period. We are aware of the large uncertainty associated with the air-sea freshwater flux (Josey and Marsh, 2005; Dee et al., 2011) and the ocean freshwater content. Therefore, we estimated both variables from two and

three databases, respectively. The difference between the ERA-Interim and NCEP estimates of accumulated air-sea freshwater flux over the two years amount to 0.4 x 10^{12} m^3, while the ocean freshwater content estimates differ by 0.3 x 10^{12} m^3 (Fig. 12). We conclude that between 70 % and 100 % of the freshening observed in the considered volume of the SPNA is caused by air-sea freshwater inputs. These results support our conclusion that the negative θ and S anomalies observed in the surface-intermediate waters during the GEOVIDE cruise were locally formed by atmospheric forcing.

More evidence for the important role of air-sea fluxes is provided by the distribution of θ, S and oxygen anomalies in the water column. Indeed, the WMLD along the OVIDE section east of 20° W coincided with the deep limit of the anomalies (Fig. 7). It is somewhat more complex in the ERRC, where the WMLD crosses the anomaly separating subpolar mode water (SPMW) and upper Labrador Sea Water (LSW), see Fig. 2b; both water masses were advected together by the ERRC, but probably issued from different ventilation regions. According to de Boisséson et al. (2012), the SPMW is formed by air-sea interactions on its way around the Iceland basin. The sign of all the anomalies described above is consistent with vertical mixing in the winter before the GEOVIDE cruise, transferring the cold, fresh and oxygenated anomalies imprinted locally by the atmosphere into the whole mixed layer. In the Irminger Sea, the WMLD in Fig. 7 reaches 1200 m although deep convection did not exceed 700 m in winter 2014 in the central Irminger Sea (Piron, 2015; Duchez et al., 2016). It most likely results from the advection in the depth range 700–1200 m of high-oxygen intermediate water with densities slightly denser than the water above and possibly formed south of Greenland, as suggested by Fig. 5.3 of Piron (2015).

Below the orange line in Fig. 7, we observed mainly warming, salinification and deoxygenation. This is in agreement with the tendencies observed since 2002 along the OVIDE section. Deep waters below 1300 m depth in the Irminger Sea were obviously not recently renewed, apart from the plume of DSOW. Kieke and Yashayaev (2015) showed the evolution of S and θ in the LSW measured in the Labrador Sea: below 1300 m, the positive tendencies of S and θ were similar to those observed in the Irminger Sea, and concerned the dense LSW formed in the 1990s.

5. Summary and conclusions

This paper addresses two main issues: first, under the umbrella of the GEOTRACES program, it contextualizes the physical background of the GEOVIDE cruise carried out in May–June 2014, which is essential for the interpretation of distribution of TEIs in the eastern SPNA. Second, it elucidates the cause of the cold and fresh anomaly detected in the surface waters of the eastern SPNA in May–June 2014.

Concerning the circulation across the OVIDE sections, the most important difference between the GEOVIDE state and the 2002–2012 mean state defined by D2016 is a strengthened Irminger Current and a weaker North Atlantic Current, with a possible transfer of volume transport from its northern branch to its central branch. The intensity of the MOC was the highest measured at the OVIDE section since 2002, 18.7 ± 3.0 Sv, and was high enough to compensate the negative temperature anomaly detected in the surface waters, resulting in a high heat transport across the OVIDE section, 0.56 ± 0.06 PW.

The special GEOVIDE stations where the trace elements were measured were indeed representative of the targeted hydrographic regions, away from the core of the main advected eddies identified along the sections. Nevertheless some precautions should be taken when comparing with previous years since temperature, salinity and oxygen of the SPNA winter mixed layer in 2014 were significantly different from the 2002–2012 mean.

Finally, we demonstrated that the cold and fresh anomalies in the 2014 mixed layer induced consistent changes in heat and freshwater content of the SPNA. This strong 2013–2014 cooling is inserted in a long-term cooling in the SPNA that started in mid-2000s. Our results elucidate the important role of air-sea flux in the θ-S changes in this region at short time-scale, overcoming the warming induced by the increase in the MOC amplitude and associated heat transport in May–June 2014.

Acknowledgements

We gratefully acknowledge the crew of the *Pourquoi Pas*? vessel for their help and assistance during the cruise and for winch repairs. We also acknowledge the work of the UTM-CSIC (Spain) technical staff for the CTD manipulation. The GEOVIDE cruise would not have been achieved without the technical skills and the commitment of Catherine Kermabon, Pierre Branellec, Philippe Le Bot, Olivier Ménage, Stéphane Leizour, Michel Hamon and Floriane Desprez de Gésincourt (LOPS) and also Fabien Pérault and Emmanuel de Saint Léger (CNRS). We are particularly grateful to Dr Géraldine Sarthou for her persistent dedication to the project and her precious advices, and to the three anonymous reviewers who greatly

helped us in improving the manuscript. The NCEP Reanalysis 2 data were provided by the NOAA/OAR/ESRL PSD, Boulder, Colorado, USA, from their web site at http://www.esrl.noaa.gov/psd/. The altimeter products were produced by Ssalto/Duacs and distributed by Aviso with support from CNES.
For this work, P. Zunino was supported by CNRS and IFREMER, within the framework of the projects AtlantOS (European Union's Horizon 2020, grant N° 633211) and GEOVIDE (ANR-13-BS06-0014-02), respectively. H. Mercier was financed by CNRS, P. Lherminier by Ifremer and N. Daniault by the University of Western Brittany, Brest. M.I. García-Ibáñez and F.F. Pérez were supported by the Spanish Ministry of Economy and Competitiveness through the BOCATS (CTM2013-41048-P) project co-funded by the Fondo Europeo de Desarrollo Regional 2014–2020 (FEDER).

References

Barrier. N., Deshayes, J., Treguier, A. M. and Cassou, C.: Heat budget in the North Atlantic subpolar gyre: Impacts of atmospheric weather regimes on the 1995 warming event, Prog. Oceanogr., 130, 75-90, doi:10.1016/j.pocean.2014.10.001, 2015.

Berrisford, P., Kallberg, P., Kobayashi, S., Dee, D., Uppala, S., Simmons, A.J., Poli, P., Sato, H.: Atmospheric conservation properties in ERA-Interim, Q. J. R. Meteorol. Soc. 137, 1381–1399. DOI:10.1002/qj.864, 2011.

Bersch, M., North Atlantic Oscillation-induced changes of the upper layer circulation in the northern North Atlantic Ocean, J. Geophys. Res.-Oceans, 107(C10), 3156, doi:10.1029/2001JC000901, 2002

Bersch, M., Yashayaev, I., Koltermann, K. P.: Recent changes of the thermohaline circulation in the subpolar North Atlantic, Ocean Dynam., 57:223–235, doi:10.1007/s10236-007-0104-7, 2007.

de Boisséson, E., Thierry, V., Mercier, H., Caniaux, G., and Desbruyères, D.: Origin, formation and variability of the Subpolar Mode Water located over the Reykjanes Ridge, J. Geophys. Res.-Oceans, 117, C12005, *doi:10.1029/2011JC007519, 2012*.

Bower, A. S. and von Appen, W.J.: Interannual variability in the pathways of the North Atlantic current over the Mid-Atlantic Ridge and the impact of topography, J. Phys. Oceanogr., 38(1), 104–120, doi:10.1175/2007JPO3686.1, 2008.

Bryden, H. and Imawaki, S.: Ocean heat transport, in: Ocean Circulation and Climate, edited by: Siedler, G., Church, J., and Gould, J., Academic Press, 2001.

Cossa, D., Heimbürger, L-E., Pérez, F. F., García-Ibáñez, M.I., Sonke, J. E., Planquette, H. , Lherminier, P., Sarthou, G.: Mercury distribution and transport in the North Atlantic Ocean along the Geotraces-*GA01 transect, Biogeosciences Discuss., doi:10.5194/bg-2017-467, 2017.*

Daniault, N., Mercier, H., Lherminier, P., Sarafanov, A., Falina, A., Zunino P., Pérez, F. F., Rios, A. F., Ferron, B., Huck, T., Thierry, V., Gladyshev, S.: The northern North Atlantic Ocean mean circulation in the early 21st Century, Prog. Oceanogr. , 146, 142-158, doi:10.1016/j.pocean.2016.06.007, 2016.

637 *Desbruyères, D., Mercier, H., Thierry, V.: On the mechanisms behind decadal heat content changes in*
638 *the eastern subpolar gyre, Prog. Oceanogr., 132, 262–272, doi:10.1016/j.pocean.2014.02.005, 2015.*

639 *Deshayes, J., and Frankignoul, C.: Simulated variability of the circulation in the North Atlantic from*
640 *1953 to 2003. J. Climate, 21, 4919–4933, doi:10.1175/2008JCLI1882.1, 2008.*

641 *Dickson, R.R., Meincke, J., Malmberg, S.A., Lee, A.J.: The ''great salinity anomaly'' in the northern*
642 *north Atlantic 1968–1982, Prog. Oceanogr., 20 (2), 103–151,* doi*: 10.1016/0079-6611(88)90049-3,*
643 *1988.*

644 *Duchez, A., Frajka-Williams, E., Josey, S. A., Evans, D. G., Grist, J. P., Marsh, R., McCarthy, G. D., Sinha,*
645 *B., Berry, D. I., and Hirschi, J. J-M: Drivers of exceptionally cold North Atlantic Ocean temperatures*
646 *and their link to the 2015 European heat wave, Environ. Res. Lett., 11, doi:10.1088/1748-*
647 *9326/11/7/074004, 2016.*

648 Frajka-Williams, E., Beaulieu, C., Duchez, A.: Emerging negative Atlantic Multidecadal Oscillation
649 index in spite of warm subtropics, Sci. Rep., doi:10.1038/s41598-017-11046-x, 2017.
650
651 *Gaillard, F., Reynaud, T., Thierry, V., Kolodziejczyk, N., Von Schuckmann, K.: In Situ–Based Reanalysis*
652 *of the Global Ocean Temperature and Salinity with ISAS: Variability of the Heat Content and Steric*
653 *Height, J. Climate, doi:10.1175/JCLI-D-15-0028.1, 2016.*

654 *García-Ibáñez, M. I., Pardo, P. C., Carracedo, L. I., Mercier, H., Lherminier, P., Ríos, A. F., and Pérez, F.*
655 *F.: Structure, transports and transformations of the water masses in the Atlantic Subpolar Gyre, Prog.*
656 *Oceanogr., 135, 18–36, doi:10.1016/j.pocean.2015.03.009, 2015.*

657 *García-Ibáñez, M. I., Pérez, F. F., Lherminier, P., Zunino, P., Tréguer, P.: Water mass distributions and*
658 *transports for the 2014 GEOVIDE cruise in the North Atlantic,* Biogeosciences
659 Discuss., doi:10.5194/bg-2017-355, 2017.
660

661 *Good, S.A., Martin, M.J. and Rayner, N. A.: EN4: quality controlled ocean temperature and salinity*
662 *profiles and monthly objective analyses with uncertainty estimate,. J Geophys. Res., 118, 6704– 6716,*
663 *doi:10.1002/2013JC009067, 2013.*

664 *Gourcuff, C., Lherminier, P., Mercier, H., and Le Traon, P. Y.: Altimetry Combined with Hydrography*
665 *for Ocean Transport Estimation, J. Atmospheric Ocean. Technol., 28(10), 1324–1337,*
666 *doi:10.1175/2011JTECHO818.1, 2011.*

667 *Grist, J. P., Josey, S. A., Jacobs, Z. L., Marsh, R., Sinha, R., Sebille, E. V. : Extreme air–sea interaction*
668 *over the North Atlantic subpolar gyre during the winter of 2013–2014 and its sub‐surface legacy,*
669 *Clim Dyn, doi:10.1007/s00382-015-2819-3, 2015.*

670 *Häkkinen, S., Rhines, P. B., and Worthen, D. L.: Warm and saline events embedded in the meridional*
671 *circulation of the northern North Atlantic. J. Geophys. Res., 116, C03006, doi:10.1029/2010JC006275,*
672 *2011.*

673 *Hátún,H., Sandø, A.B., Drange, H., Hansen, B., and Valdimarsson, H.: Influence of the Atlantic*
674 *subpolar gyre on the Thermohaline circulation. Science, 309, 1841–1844,*
675 *doi:10.1126/science.1114777, 2005.*

Hermanson, L., Eade, R., Robinson, N. H., Dunstone, N. J., Andrews, M. B., Knight, J. R., Scaife, A. A., and Smith, D. M.: Forecast cooling of the Atlantic subpolar gyre and associated impacts, Geophys. Res. Lett., 41, 5167–5174, doi:10.1002/2014GL060420, 2014.

Holliday, N. P., Cunningham, S. A., Johnson, C., Gary, S. F., Griffiths, C., Read, J. F., and Sherwin, T.: Multidecadal variability of potential temperature, salinity, and transport in the eastern subpolar North Atlantic, J. Geophys. Res. Oceans, 120, 5945– 5967, doi:10.1002/2015JC010762, 2015.

Hosoda, S., Ohira, T. and Nakamura, T.: A monthly mean dataset of global oceanic temperature and salinity derived from Argo float observations, JAMSTEC Rep. Res. Dv., 8, 47- 59, 2008.

Hurrell, James & National Center for Atmospheric Research Staff (Ed). Last modified 06 Oct 2017. "The Climate Data Guide: Hurell North Atlantic Oscillation (NAO) Index (station-based)". https://climatedateguide.ucar.edu/climate-data/hurrell-north-atlantic-oscillation-nao-index-stationèbased.

IPCC, 2007: Climate Change 2007: The Physical Science Basis. Contribution of Working Group I to the Fourth Assessment Report of the Intergovernmental Panel on Climate Change [Solomon, S., D. Qin, M. Manning, Z. Chen, M. Marquis, K.B. Averyt, M. Tignor and H.L. Miller (eds.)]. Cambridge University Press, Cambridge, United Kingdom and New York, NY, USA, 996 pp.

Johnson, G. C., Lyman, J. M., Boyer, T., Domingues, C. M., Ishii, M., Killick, R., Monselesan, D., and Wijffels, S. E.: Ocean heat content [in "State of the Climate in 2015"]. Bull. Amer. Meteor. Soc., 97 (8), S64–S65, 2016.

Josey, S. A., and Marsh, R.: Surface freshwater flux variability and recent freshening of the North Atlantic in the eastern subpolar gyre, J. Geophys.-Res., VOL. 110, C05008, doi:10.1029/2004JC002521, 2005.

Kalnay, E., Kanamitsu, M., Kistler, R.: The NCEP/NCAR 40-year reanalysis project. Bulletin of the American Meteorological Society 77, 437–470, 1996

Kanamitsu, M., Ebisuzaki, W., Woollen, J., Yang, S.-K., Hnilo, J. J., Fiorino, M., and Potter, G.L.: NCEP–DOE AMIP-II Reanalysis (R-2). Bulletin of the American Meteorological Society 83:1631–1643, 2002.

Kieke, D. and Yashayaev, I.: Studies of Labrador Sea Water formation and variability in the subpolar North Atlantic in the light of international partnership and collaboration, Prog. Oceanogr., 132, 220–232, doi:10.1016/j.pocean.2014.12.010, 2015.

Khatiwala, S., Tanhua T., Mikaloff Fletcher S., Gerber M., Doney S.C., Graven H. D., Gruber N., McKinley G.A., Murata A., Rios A.F. and Sabine C.L.: Global ocean storage of anthropogenic carbon. Biogeosicences, 10, 2169-2191, doi:10.5194/bg-10-2169-2013, 2013.

Kuhlbrodt, T., Griesel, A., Montoya, M., Levermann, A., Hofmann, M., and Rahmstorf, S.: On the driving processes of the Atlantic meridional overturning circulation, Rev. Geophys., 45, RG2001, doi:10.1029/2004RG000166, 2007.

Lemaître, N., Planquette, H., Planchon, F., Sarthou, G., Jacquet, S., García-Ibáñez, M.I, Gourain, A., Cheize,M., Monin, L., André, L., Laha, P., Terryn, H., Dehairs, F. : Particulate barium tracing significant

718 mesopelagic carbon remineralisation in the North Atlantic, Biogeosciences
719 Discuss., doi:10.5194/bg-2017-400, 2017

720

721 *Lherminier, P., Mercier, H., Gourcuff, C., Alvarez, M., Bacon, S., and Kermabon, C.: Transports across*
722 *the 2002 Greenland-Portugal Ovide section and comparison with 1997, J. Geophys. Res.,*
723 *112(C07003), doi:10.1029/2006JC003716, 2007.*

724 *Lherminier, P., Mercier, H., Huck, T., Gourcuff, C., Pérez, F. F., Morin, P., Sarafanov, A., and Falina, A.:*
725 *The Atlantic Meridional Overturning Circulation and the subpolar gyre observed at the A25-OVIDE*
726 *section in June 2002 and 2004, Deep-Sea Res. Part -Oceanogr. Res. Pap., 57(11), 1374–1391,*
727 *doi:10.1016/j.dsr.2010.07.009, 2010.*

728 *Levitus, S., Antonov, J. I., Boyer, T. P., Baranova, O. K., Garcia, H. E., Locarnini, R. A., Mishonov, A. V.,*
729 *Reagan, J. R., Seidov, D., Yarosh, E. S., and Zweng, M. M.: World ocean heat content and*
730 *thermosteric sea level change (0–2000 m), 1955–2010, Geophys. Res. Let., 39, L10603,*
731 *doi:10.1029/2012GL051106, 2012.*

732 *Lohmann, K., Drange, H., and Bentsen, M.: Response of the North Atlantic subpolar gyre to persistent*
733 *North Atlantic Oscillation like forcing, Climate Dyn., 32, 273–285, doi:10.1007/s00382-008-0467-6,*
734 *2009.*

735 *Lux, M., Mercier, H., and Arhan, M.: Interhemispheric exchanges of mass and heat in the Atlantic*
736 *Ocean in January–March 1993, Deep-Sea Res. Pt. I, 48, 605–638, 2001.*

737 *Marsh, R., Josey, S. A., de Cuevas, B. A., Redbourn, L. J. and Quartly, G. D.: Mechanisms for recent*
738 *warming of the NorthAtlantic: Insights gained with an eddy-permitting model, J. Geophys. Res., 113,*
739 *C04031, doi:10.1029/2007JC004096, 2008.*

740 *Mercier, H.: Determining the general circulation of the ocean: a non linear inverse problem, J.*
741 *Geophys. Res., 91, 5103–5109, doi:10.1029/JC091iC04p05103, 1986.*

742 *Mercier, H., Lherminier, P., Sarafanov, A., Gaillard, F., Daniault, N., Desbruyères, D., Falina, A., Ferron,*
743 *B., Gourcuff, C., Huck, T., Thierry,V.: Variability of the meridional overturning circulation at the*
744 *Greenland–Portugal OVIDE section from 1993 to 2010, Prog. Oceanogr., 132, 250–261,*
745 *doi:10.1016/j.pocean.2013.11.001, 2015.*

746 *Pérez, F. F., Mercier, H., Vázquez-Rodríguez, M., Lherminier, P., Velo, A., Pardo P. C., Rosón, G. and*
747 *Ríos, A. F.: Atlantic Ocean CO_2 uptake reduced by weakening of the meridional overturning*
748 *circulation. Nat. Geosci., doi:10.1038/NGEO1680, 2013.*

749 *Pérez, F. F., Vázquez-Rodríguez, M., Mercier, H., Velo, A., Lherminier, P. and Ríos, A.F.: Trends of*
750 *anthropogenic CO_2 storage in North Atlantic water masses. Biogeosciences, 7, 1789 – 1807,*
751 doi:10.5194/bg-7-1789-2010, 2010

752 *Piron, A.: Observation de la convection profonde en mer d'Irminger sur la période 2002-2015 par les*
753 *flotteurs Argo, PhD Thesis, Université de Bretagne Occidentale.*
754 *http://archimer.ifremer.fr/doc/00313/42434/, 2015.*

Piron, A., Thierry, V., Mercier, H., and Caniaux, G.: Gyre-scale deep convection in the subpolar North Atlantic Ocean during winter 2014–2015, Geophys. Res. Lett., 44, 1439–1447, doi:10.1002/2016GL071895, 2017.

Rhein, Monika., Kieke, D., Hüttl-Kabus, S., Roessler, A., Mertens, C., Meissner, R., Klein, B., Böning, CW., Yashayaev, I.: Deep water formation, the subpolar gyre, and the meridional overturning circulation in the subpolar North Atlantic, Deep-Sea Research II, 58, 1819–1832, doi:10.1016/j.dsr2.2010.10.061, 2011.

Riser, S. C., Freeland, H. J., Roemmich, D., Wijffels, S., Troisi, A., Belbeoch, M., Gilbert, D., Xu, J., Pouliquen, S., Ann, T., Le Traon, P. Y., Maze, G., Klein, B., Ravichandran M., Grant, F., Poulain, P. M., Suga, T., Lim, B., Sterl. A., Sutton, P., Mork, K. A., Velez-Belch, J. P., Ansorge, I., King, B., Turton, J., Baringer, M., Jayne, S. R.: Fifteen years of ocean observations with the global Argo array . Nat. Clim. Change, 6(2), 145-153 . doi:10.1038/NCLIMATE2872, 2016.

Robson, J., Sutton, R., Lohmann, K.,Smith., D., and Palmer, M.: Causes of the Rapid Warming of the North Atlantic Ocean in the Mid-1990s, J. Climate, doi:10.1175/JCLI-D-11-00443.1, 2012.

Robson, J., Sutton, R. and Smith, D.: Decadal predictions of the cooling and freshening of the North Atlantic in the 1960s and the role of ocean circulation, Clim. Dyn., 42, 2353–2365, doi:10.1007/s00382-014-2115-7, 2014.

Robson, J., Ortega, P., Sutton, R.: A reversal of climatic trends in the North Atlantic
since 2005, Nature Geo., DOI: 10.1038/NGEO2727, 2016.

Robson, J., Polo, I., Hodson, D. L. R., Stevens, D. P., Shaffrey, L. C.: Decadal prediction of the NorthAtlantic subpolar gyre in the HiGEM high‐resolution climate model, Clim. Dyn., DOI: 10.1007/s00382-017-3649-2, 2017.

Rossby, T., Reverdin, G., Chafik, L., and Søiland, H.: A direct estimate of poleward volume, heat, and freshwater fluxes at 59.58N between Greenland and Scotland. J. Geophys. Res.-Oceans, doi:10.1002/2017JC012835, 2017.

Sarafanov, A., Falina, A., Sokov, A., and Demidov, A.: Intense warming and salinification of intermediate waters of southern origin in the eastern subpolar North Atlantic in the 1990s to mid-2000s, J. Geophys. Res., 113, C12022, doi:10.1029/2008JC004975, 2008.

Sarafanov, A., A. Falina, H. Mercier, A. Sokov, P. Lherminier, C. Gourcuff, S. Gladyshev, F. Gaillard, and N. Daniault (2012), Mean full-depth summer circulation and transports at the northern periphery of the Atlantic Ocean in the 2000s, J. Geophys. Res.-Oceans, 117(C01014), doi:10.1029/2011JC007572, 2012.

Sgubin G., Swingedouw D., Drijfhout S., Mary Y. and Bennabi A.: Abrupt cooling over the North Atlantic in modern climate models, Nat. Commun., 8, 14375, doi: 10.1038/ncomms14375, 2017.

Spall, M. A. and Price, J. F.: Mesoscale Variability in Denmark Strait: The PV Outflow Hypothesis, J. Phys. Oceanogr., 1997.

Väge, K., Pickart, R. S., Sarafanov, A., Knutsen, O., Mercier, H., Lherminier, P., van Aken, H. M., Meincke, J., Quadfasel, D., and Bacon, S.: The Irminger Gyre: Circulation, convection, and interannual

variability, Deep-Sea Res. Part -Oceanogr. Res. Pap., 58(5), 590–614, doi:10.1016/j.dsr.2011.03.001, 2011.

Williams, R., Roussenov, V., Smith, D., Lozier, S.: Decadal evolution of ocean thermal anomalies in the North Atlantic: The effects of Ekman, Overturning, and Horizontal Transport, J. Climate, 27, doi:10.1175/JCLI-D-12-00234.1, 2014.

Yashayaev, I., and Loder, J. W.: Recurrent replenishment of Labrador Sea Water and associated decadal scale variability, J. Geophys. Res. Oceans, 121, 8095–8114, doi:10.1002/2016JC012046, 2016.

Yashayaev, I., and Loder J. W.: Further intensification of deep convection in the Labrador Sea in 2016, Geophys. Res. Lett., 44, 1429–1438, doi:10.1002/2016GL071668, 2017.

Zunino, P., Pérez, F. F., Fajar, N. M., Guallart, E. F., Ríos, A. F., Pelegrí, J. L., and Hernández-Guerra, A.: Transports and budgets of anthropogenic CO_2 in the tropical North Atlantic in 1992–1993 and 2010–2011, Global Biogeochem. Cycles, 29, 1075–1091, doi:10.1002/2014GB005075, 2015.

TABLES

Table 1. Intensity (top-to-bottom integrated) of the different dynamical structures defined in section 3.1 for 2014 and the mean values (2002–2012) estimated by Daniault et al. (2016). Note that the errors given for the GEOVIDE estimates come from the covariance matrix resulting from the inverse model. Otherwise, the errors given with the mean values are the standard deviation of the six estimates of each current.

Units: Sv	WBC	IG	IC		ERRC	NAC	Recirculation
			as D2016	Northward transport			
GEOVIDE	-30.3 ± 2.1	6.8 ± 3.0	17.5 ± 7.3	22.7 ± 6.5	-13.6 ± 6.0	32.2 ± 11.4	-10.2 ± 6.4
MEAN (2002–2012)	-33.1 ± 2.6	7.7 ± 2.1	9.5 ± 3.4	11.0 ± 3.4	-12.1 ± 1.1	41.8 ± 3.7	-13.0 ± 2.0

FIGURE CAPTIONS

Fig. 1. Schematic diagram of the 2002–2012 mean large-scale circulation adapted from Daniault et al. (2016). Bathymetry is plotted in color with color changes at 100 m, 1000 m and every 1000 m below 1000 m. The locations of the GEOVIDE hydrographic stations are indicated by black dots along the OVIDE section and across the Labrador Sea. Red dots, and associated numbers, along the OVIDE section show the stations delimiting the regions used in this paper for the transport computations of the different currents crossing the OVIDE section. The names of the main currents are indicated in the figure: East Greenland-Irminger Current (EGIC), Deep Western Boundary Current (DWBC), Irminger Current (IC), Eastern Reykjanes Ridge Current (ERRC), Northern branch of the North Atlantic Current (NNAC), Subarctic Front (SAF) and Southern branch of the North Atlantic Current (SNAC). Superstations and XL stations carried out during GEOVIDE are represented by pink stars. The main topographical features of the Subpolar North Atlantic are labeled: Azores-Biscay Rise (ABR), Bight Fracture Zone (BFZ), Charlie–Gibbs Fracture Zone (CGFZ), Faraday Fracture Zone (FFZ), Maxwell Fracture Zone (MFZ), Mid-Atlantic Ridge (MAR), Iberian Abyssal Plain (IAP), Northwest Corner (NWC), Rockall Trough (RT), Rockall Plateau (Rockall P.) and Maury Channel (MC). The main water masses are indicated: Denmark Strait Overflow Water (DSOW), Iceland–Scotland Overflow Water (ISOW), Labrador Sea Water (LSW), Mediterranean Water (MW), and Lower North East Atlantic Deep Water (LNEADW).

Fig. 2. Vertical section of potential temperature (°C), salinity and oxygen (µmol kg^{-1}) along the OVIDE section measured during the GEOVIDE cruise. The horizontal grey lines in the three plots represent the isopycnal layers (σ_1 = 32.15 kg m^{-3}, σ_0 = 27.80 kg m^{-3} or σ_2 = 36.94 kg m^{-3}, σ_4 = 45.85 kg m^{-3}) indicated in the upper plot. The vertical grey lines in the three plots are the limits between the different circulation components crossing the OVIDE section: Western Boundary Current (WBC), Irminger Gyre (IG), Irminger Current (IC), Eastern Reykjanes Ridge Current (ERRC), northern branch of the North Atlantic Current (NNAC), SubArctic Front (SAF), southern branch of the North Atlantic Current (SNAC) and the recirculation in the Iberian Abyssal Plain (RECIR.). The main water masses are indicated in the central plot: Denmark Strait Overflow Water (DSOW), Iceland–Scotland Overflow Water (ISOW), Labrador Sea Water (LSW), Sub-Polar Mode Water (SPMW), Sub-Arctic Intermediate Water (SAIW), North Atlantic Central Water (NACW), Mediterranean Water (MW) and North East Atlantic Deep Water (NEADW). The main topographic features are indicated in the bottom

plot: Reykjanes Ridge (RR), Eriador Seamount (ESM), Western European Basin (WEB), Azores-Biscay Rise (ABR) and Iberian Abyssal Plain (ABP). Ticks at the top of the upper and central plots indicate the positions of all the stations measured during GEOVIDE, along the OVIDE section, with some station numbers given above. In the bottom plot, the red and green numbers indicate the position of the superstations and XLarge stations, respectively.

Fig. 3. Velocities (m s^{-1}) orthogonal to the OVIDE section measured during the GEOVIDE cruise. Positive/negative values indicate northeastward/southwestward velocities. a) Velocities measured by the ship-ADCP. b) Geostrophic velocity obtained by the inversion model plus Ekman velocities in the upper 30 m. The vertical black lines are the limits between the different circulation components crossing the OVIDE section as defined in the main text and at the bottom of Fig. 2a. The horizontal discontinuous black line delimits the 800 dbar for comparison of Fig. 3a and 3b. The horizontal black continuous lines are the isopycnals σ_1 = 32.15 kg m^{-3}, σ_0 = 27.80 kg m^{-3} or σ_2 = 36.94 kg m^{-3} and σ_4 = 45.85 kg m^{-3}. Bold numbers inside the figure are the volume transports (in Sv) estimated for each region and vertical layer, with errors in parentheses. The only exception is the estimation of the IG transport, which, following Väge et al. (2011) was computed as the northward transport (the 0 m s^{-1} isotach is indicated as a thin black line in Fig. 3b in the western Irminger Sea). Station numbers at the top of the figure are color-coded: black for regular stations, blue for large stations, green for XLarge stations and red for superstations. The eddies described in section 3.2 are indicated at the top of the plots.

Fig. 4. Upper pannel: Stream function or volume transport horizontally accumulated from Greenland to each GEOVIDE station, down to Portugal, and vertically accumulated in the upper limb of the MOC (red discontinuous line) and in the whole water column (red continuous line). The mean salinity in the upper limb of the MOC is also shown by the blue line and labeled on the right-hand axis. Acronyms in the top of the figure indicate the different components of the circulation crossing the OVIDE section as defined in Fig. 2. See Fig. 3 for station numbers and bathymetry legend. Lower pannel: bathymetry along the OVIDE section; acronyms as in Fig. 2

Fig. 5. Surface velocities (m s^{-1}) derived from AVISO data: arrows indicate current direction and colors indicate current intensity. The white line represents the OVIDE section. The red and white points indicate the extension of the different dynamical structures crossing the OVIDE section in 2014. The white points delimit the extension of the NAC. The pink stars indicate the position of the GEOVIDE superstations and XLarge stations. The bathymetry contours, every 1000 m, are indicated by light white lines.

Fig. 6. Surface velocities derived from AVISO data, as in Fig. 5, but zooming in on the NAC region in March 2014, April 2014, May 2014 and June 2014. The yellow, red, clear green and orange squares indicate the position of the northern, central and southern eddies, respectively, discussed in section 3.2. The numbers of the GEOVIDE stations are indicated in all the plots: pink for the superstations and XLarge stations, and yellow for regular stations. The red and green points delimitate the position of the SAF and the NAC, respectively, at the period of the GEOVIDE cruise. The bathymetry contours, every 1000 m, are indicated by light white lines.

Fig. 7. Anomalies of potential temperature (upper panel, in °C), salinity (middle panel) and oxygen (bottom panel, in µmol kg^{-1}) in 2014 with respect to the OVIDE 2002–2012 mean. Only anomalies larger than one standard deviation of the 2002–2012 values are colored in the figure. Station numbers follow the color code of Fig. 2. The orange line indicates the winter mixed-layer depth (WMLD); in the Irminger Sea, the dotted line indicates the WMLD that was not formed locally (see section 4.2). The acronyms in the bottom plot are as in Figs. 2 and 3.

Fig. 8. Contours of the Absolute Dynamical Topography (ADT) averaged over 2014 (in thin lines), contours are every 0.05 m. Thick contours correspond to the levels encompassing the SAF front during OVIDE cruises: red for the mean 2002–2012 and black for 2014. Note that the temporal trend on the mean ADT over the whole box (2.8 mm yr^{-1}) was removed. Bathymetry (1000 m step contours) and the OVIDE section are plotted in white. Colors represent the absolute velocity of the current (yellow for velocities stronger than 0.3 m s^{-1}).

Fig. 9. Heat content anomalies with respect to the mean heat content for the period 2002 – 2012 in the upper 1000 m of the region 40–60 °N and 45–10 °W: the monthly time series in grey and the 2-year running mean in black. Data source: EN4 database (Good et al., 2013). The red square highlights the short-term cooling event analyzed in this paper.

Fig. 10. Annual mean anomalies of potential temperature (left panel) and salinity (right panel) in the surface waters (20–500 m) in the North Atlantic, estimated from ISAS database. The reference period for estimating the anomalies was 2002–2012. The OVIDE section is represented by a black line. Only anomalies larger than one standard deviation are colored in the figure.

Fig. 11. 2014 Winter–Spring (DJFMAM) mean anomalies. The anomalies were calculated in with respect to the period 2002–2012. A, B and C are the total heat, sensible heat and latent heat air-sea flux, respectively, in W m^{-2}; positive/negative values indicate ocean heat gain/lost. D, E and F are net gain of freshwater, evaporation and precipitation; the unit is 10^{-4} m; positive/negative values indicate ocean freshwater gain/loss. The contours of anomalies 0 W m^{-2} (in a, b and c) and of 0 m (in d, e and f) are represented by a white line. Data source: ERA-Interim. The green square represents the area for which the changes of heat/freshwater content, and the integrated air-sea heat/freshwater flux represented in Fig. 12 were evaluated.

Fig. 12. Monthly time series of the freshwater content change between one month and the month before (in m^3), accumulated since February 1, 2013 in the upper 1000 m of the box delimited by 40–60 °N and 45–10 °W computed from three datasets: EN4 (blue), ISAS (red) and JAMSTEC (green). Integrated air-sea freshwater flux, or precipitation minus evaporation, over the same box, and accumulated from January 16, 2013, from ERA-Interim (continuous black line) and from NCEP (discontinuous black line) databases.

Fig. 1

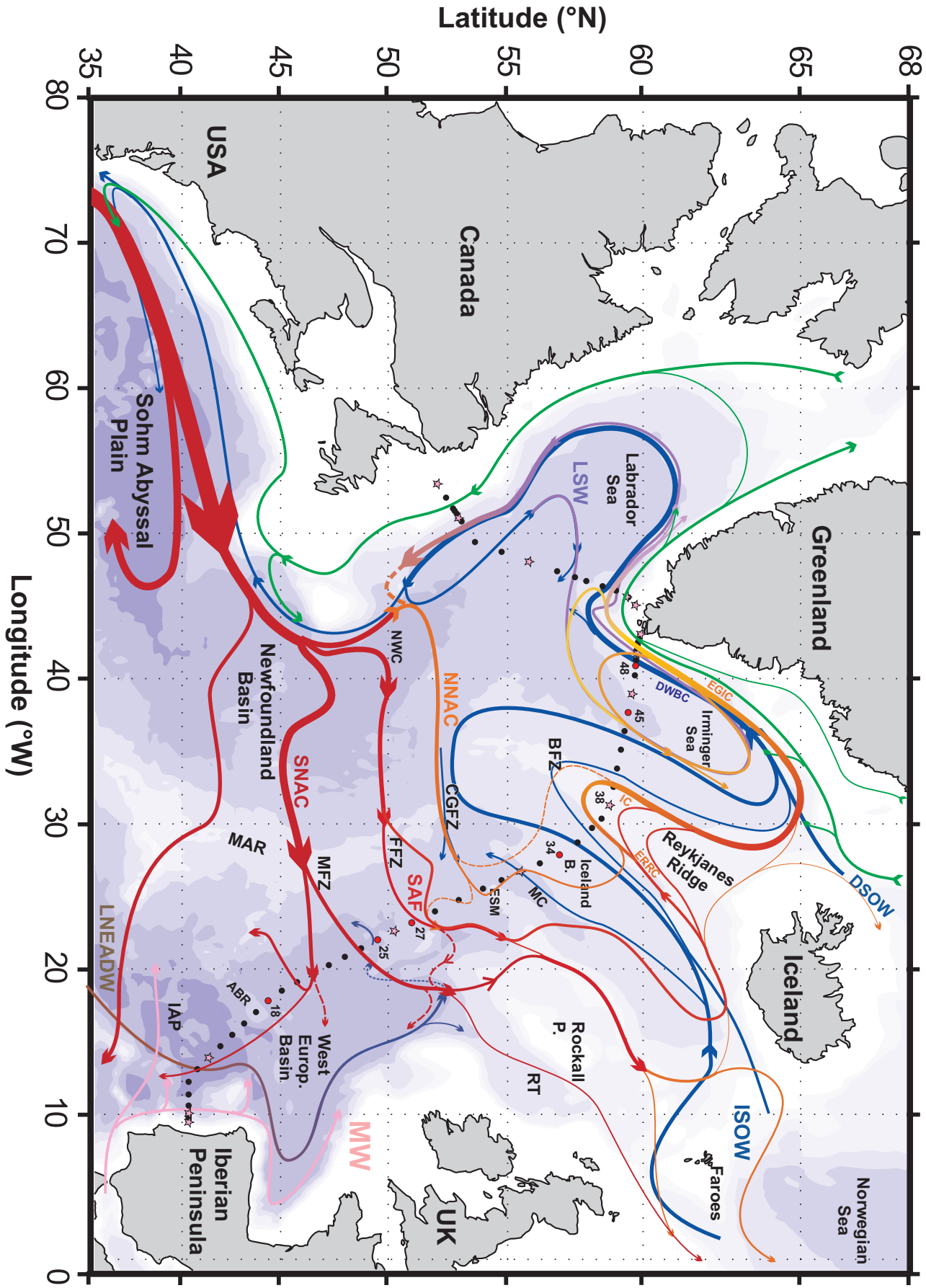
Latitude (°N)
Longitude (°W)
USA
Canada
Greenland
Iceland
Faroes
UK
Iberian Peninsula
Norwegian Sea
Sohm Abyssal Plain
Labrador Sea
LSW
Irminger Sea
DWBC
EGIC
DSOW
ISOW
NWC
NNAC
SNAC
CGFZ
BFZ
IC
ERRC
Reykjanes Ridge
Iceland B.
MC
ESM
FFZ
SAF
MFZ
MAR
Newfoundland Basin
LNEADW
MW
RT
Rockall P.
West Europ. Basin
IAP
ABR
48
45
38
34
27
25
18

Fig. 2

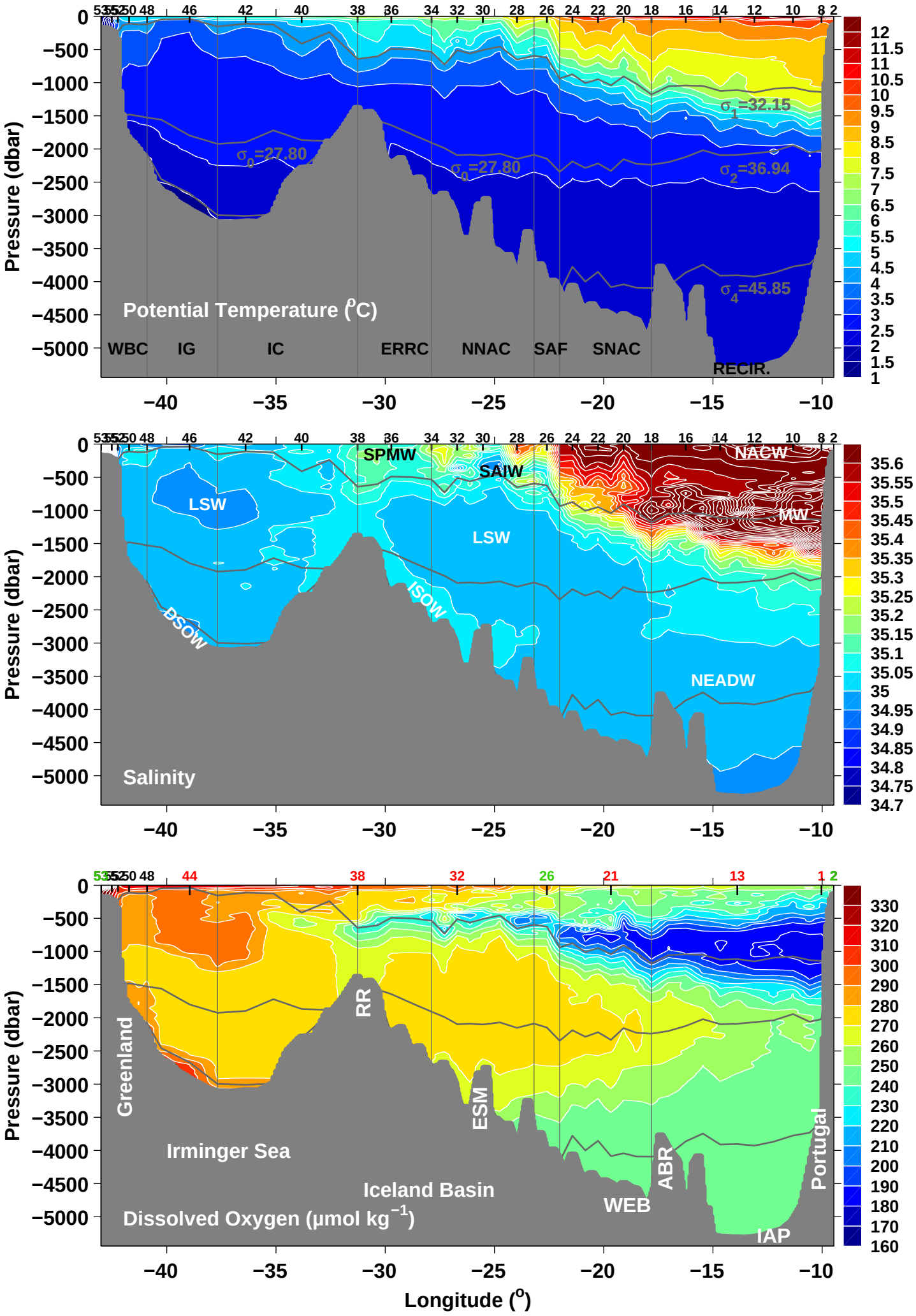
Pressure (dbar)
Potential Temperature (°C)
σ0=27.80
σ0=27.80
σ1=32.15
σ2=36.94
σ4=45.85
WBC
IG
IC
ERRC
NNAC
SAF
SNAC
RECIR.
Salinity
SPMW
SAIW
NACW
MW
LSW
LSW
ISOW
DSOW
NEADW
Greenland
Irminger Sea
RR
ESM
Iceland Basin
WEB
ABR
Portugal
IAP
Dissolved Oxygen (μmol kg−1)
Longitude (°)

Fig. 3

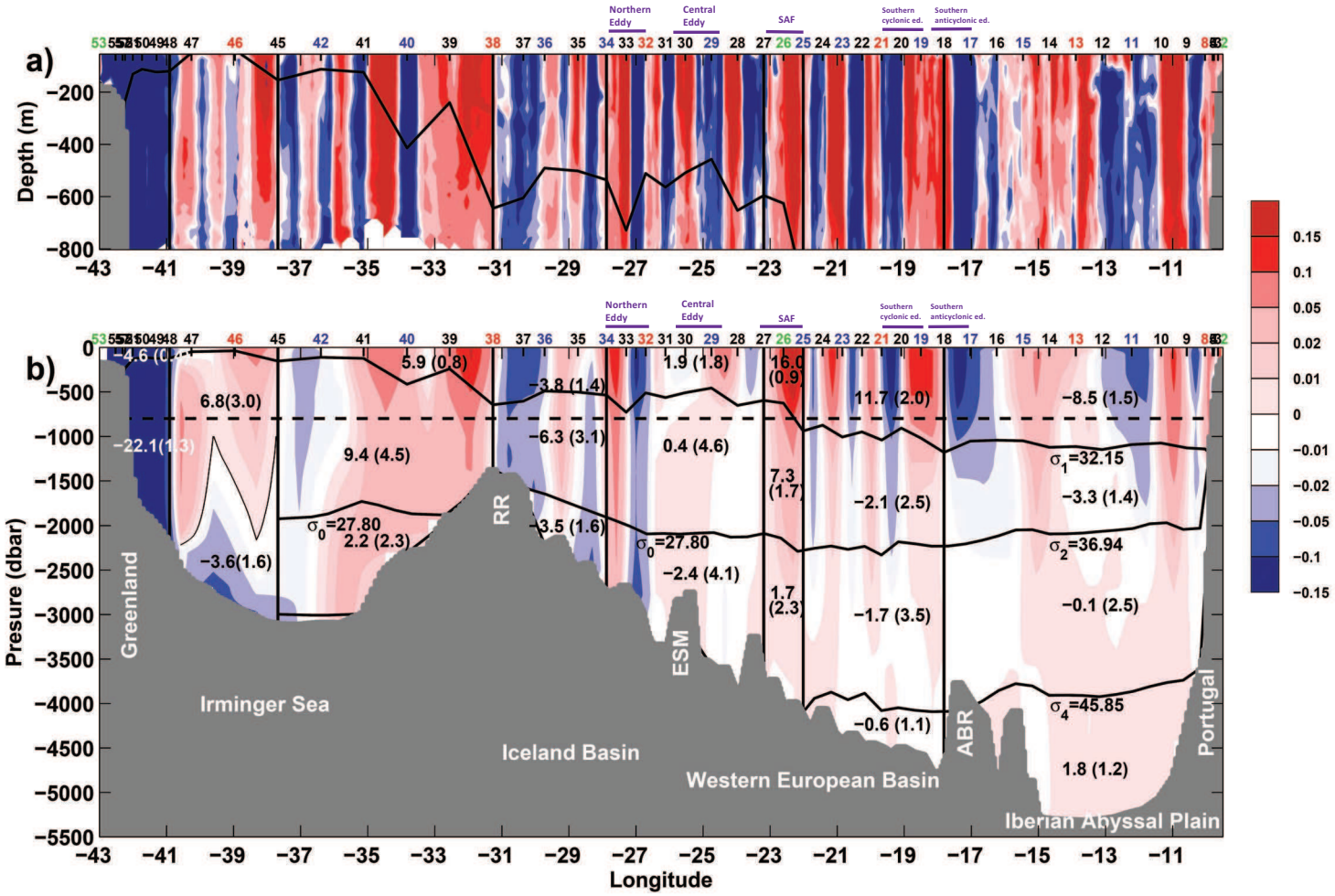
a)
b)
Depth (m)
Presure (dbar)
Longitude
Northern Eddy
Central Eddy
SAF
Southern cyclonic ed.
Southern anticyclonic ed.
Greenland
Irminger Sea
Iceland Basin
RR
ESM
Western European Basin
ABR
Portugal
Iberian Abyssal Plain
σ0=27.80
σ1=32.15
σ2=36.94
σ4=45.85
6.8(3.0)
5.9 (0.8)
-3.8 (1.4)
1.9 (1.8)
16.0 (0.9)
11.7 (2.0)
-8.5 (1.5)
9.4 (4.5)
-6.3 (3.1)
0.4 (4.6)
7.3 (1.7)
-2.1 (2.5)
-3.3 (1.4)
2.2 (2.3)
-3.5 (1.6)
-3.6(1.6)
-2.4 (4.1)
1.7 (2.3)
-1.7 (3.5)
-0.1 (2.5)
-0.6 (1.1)
1.8 (1.2)
0.15
0.1
0.05
0.02
0.01
0
-0.01
-0.02
-0.05
-0.1
-0.15

Fig. 4

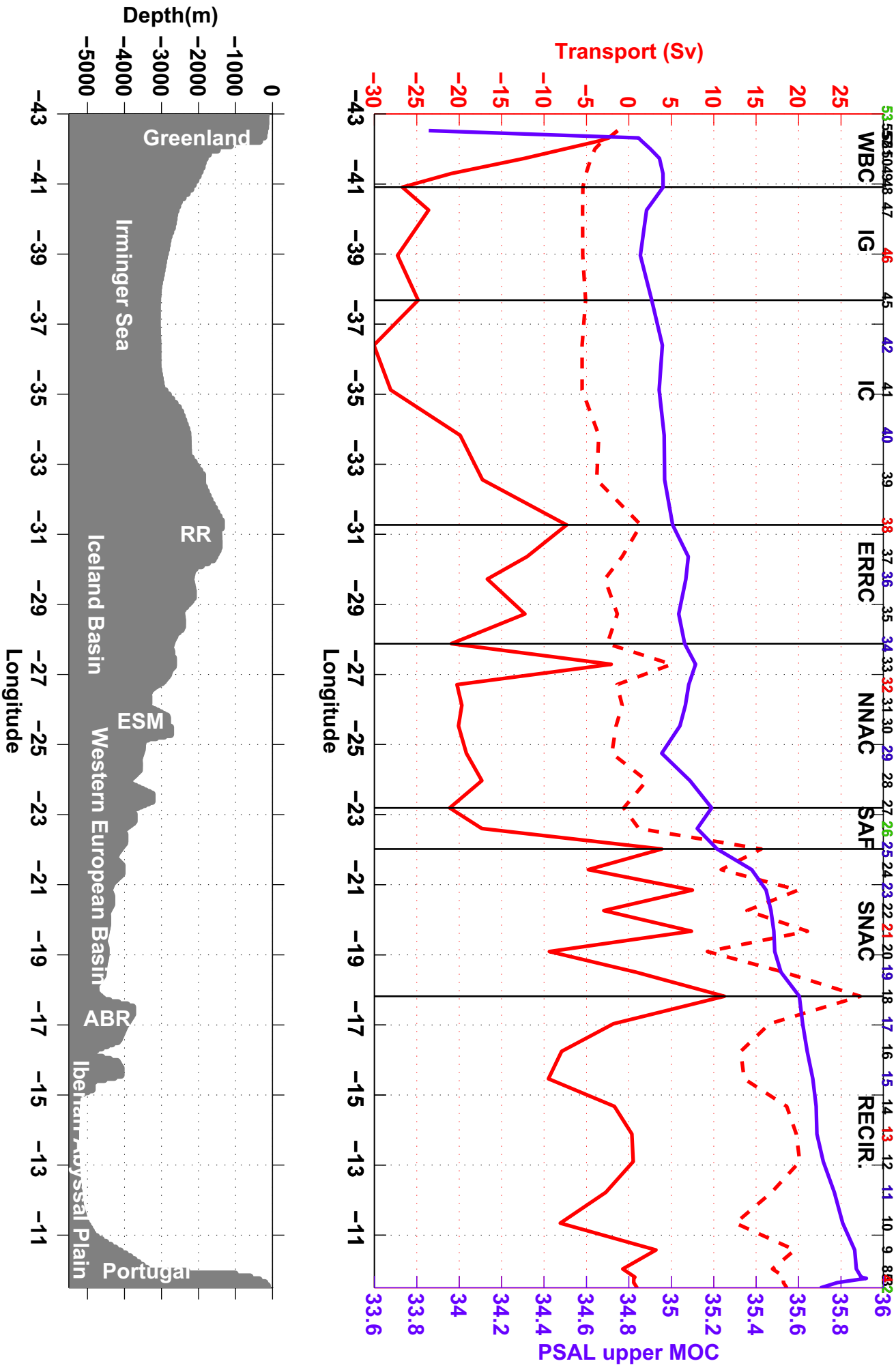
Depth(m)
0
−1000
−2000
−3000
−4000
−5000
Greenland
Irminger Sea
Iceland Basin
RR
ESM
Western European Basin
ABR
Iberian Abyssal Plain
Portugal
Longitude
−43 −41 −39 −37 −35 −33 −31 −29 −27 −25 −23 −21 −19 −17 −15 −13 −11
Transport (Sv)
25 20 15 10 5 0 −5 −10 −15 −20 −25 −30
WBC
IG
IC
ERRC
NNAC
SAF
SNAC
RECIR.
PSAL upper MOC
35.8 35.6 35.4 35.2 35 34.8 34.6 34.4 34.2 34 33.8 33.6

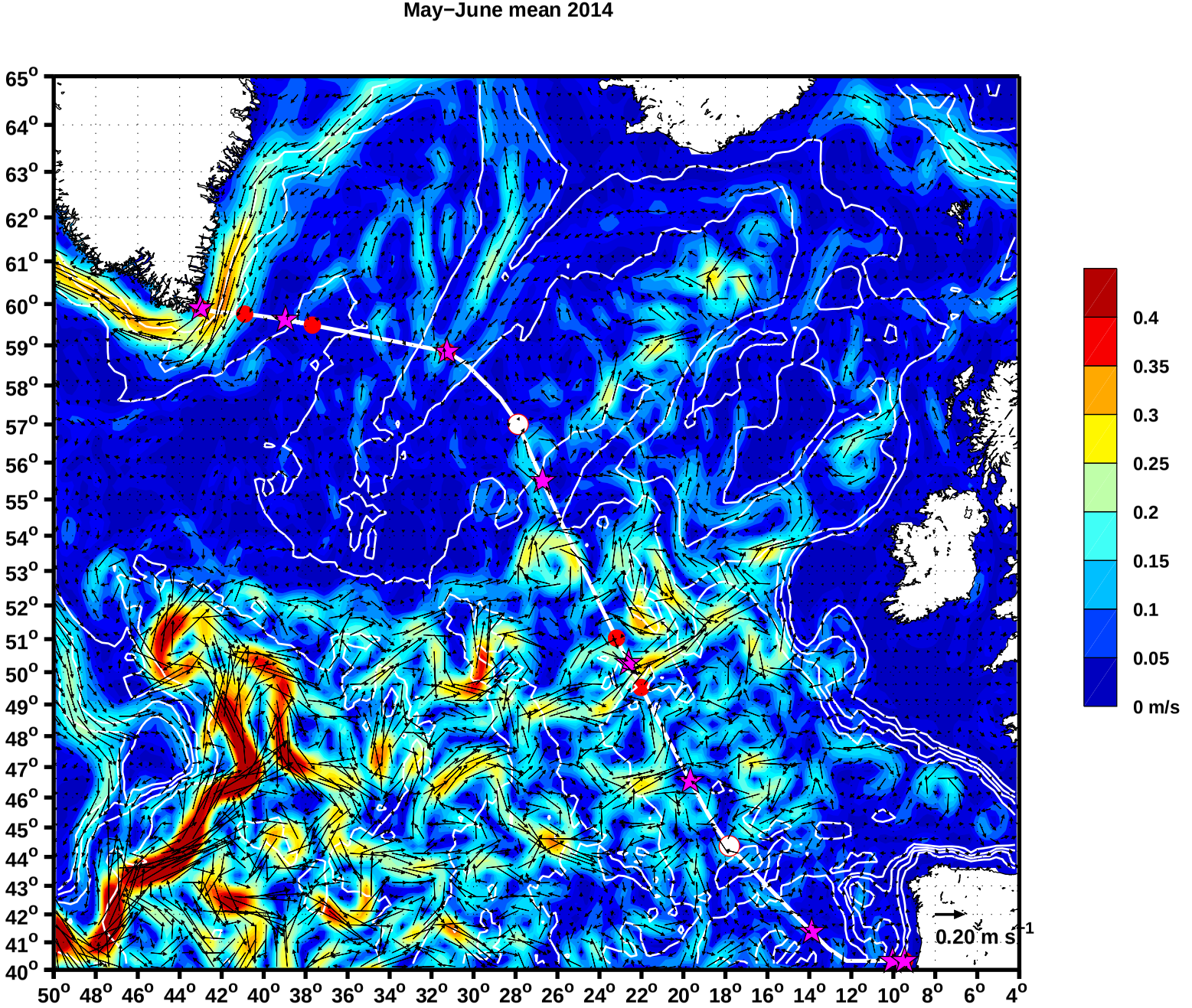
May−June mean 2014
65° 64° 63° 62° 61° 60° 59° 58° 57° 56° 55° 54° 53° 52° 51° 50° 49° 48° 47° 46° 45° 44° 43° 42° 41° 40°
50° 48° 46° 44° 42° 40° 38° 36° 34° 32° 30° 28° 26° 24° 22° 20° 18° 16° 14° 12° 10° 8° 6° 4°
0.4
0.35
0.3
0.25
0.2
0.15
0.1
0.05
0 m/s
0.20 m s-1

Fig. 5

Fig. 6

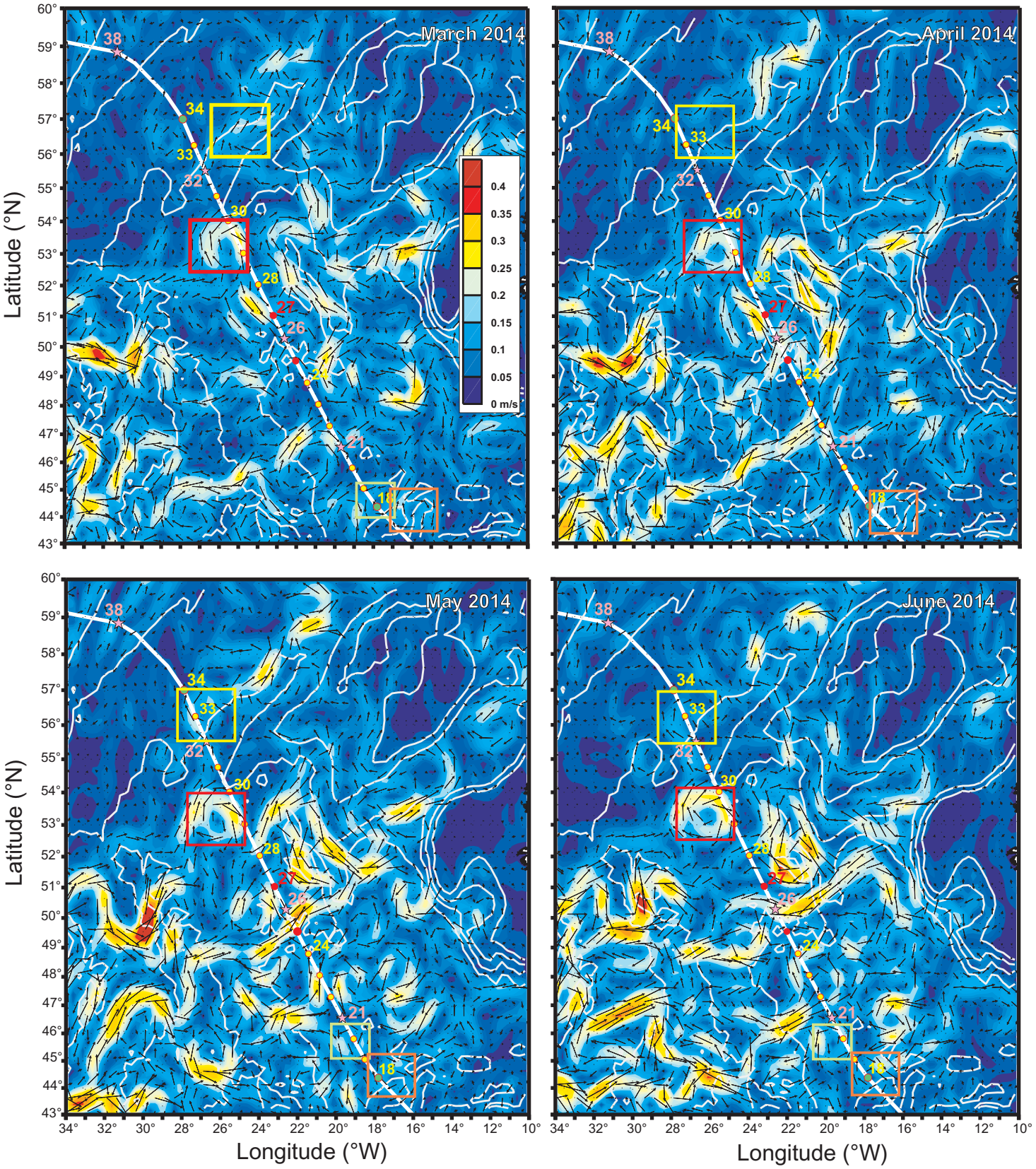
March 2014
April 2014
May 2014
June 2014
0.4
0.35
0.3
0.25
0.2
0.15
0.1
0.05
0 m/s
Latitude (°N)
Longitude (°W)
38
34
33
32
30
28
27
26
24
21
18

Fig. 7

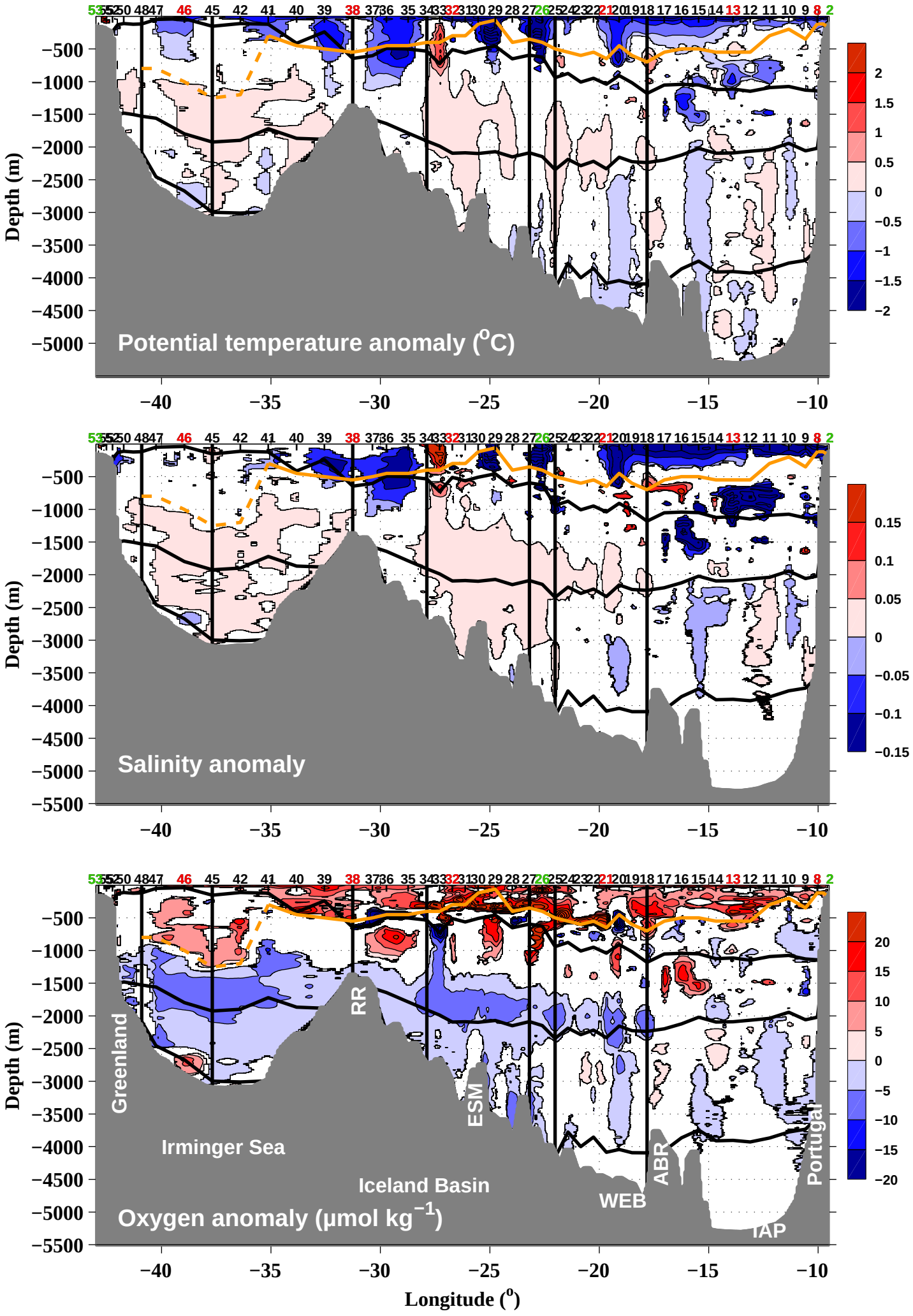
Depth (m)
Potential temperature anomaly (°C)
Salinity anomaly
Oxygen anomaly (µmol kg⁻¹)
Greenland
Irminger Sea
RR
ESM
Iceland Basin
WEB
ABR
Portugal
IAP
Longitude (°)

Fig. 8

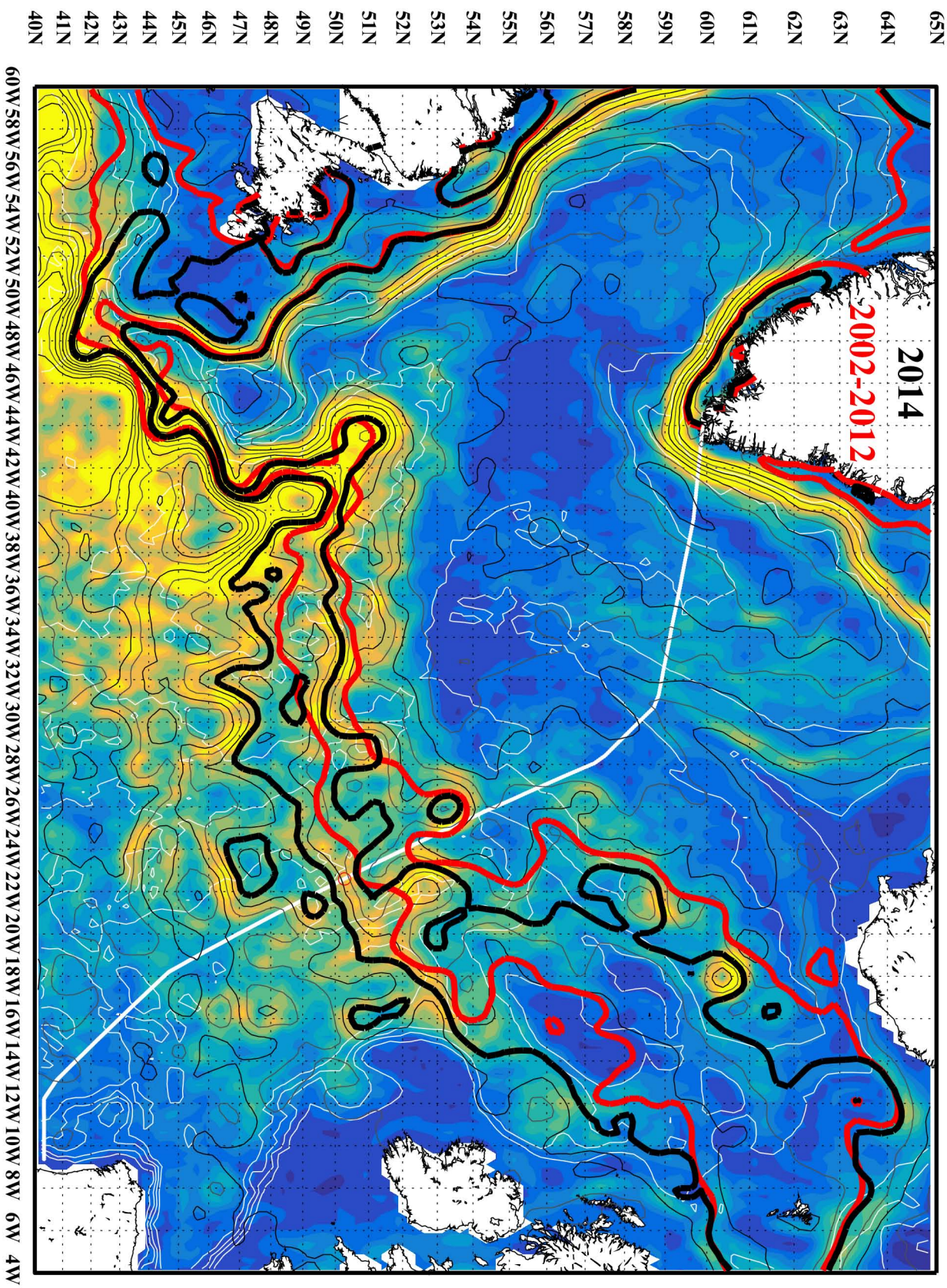
2014
2002-2012
65N
64N
63N
62N
61N
60N
59N
58N
57N
56N
55N
54N
53N
52N
51N
50N
49N
48N
47N
46N
45N
44N
43N
42N
41N
40N
60W 58W 56W 54W 52W 50W 48W 46W 44W 42W 40W 38W 36W 34W 32W 30W 28W 26W 24W 22W 20W 18W 16W 14W 12W 10W 8W 6W 4W

Fig. 9

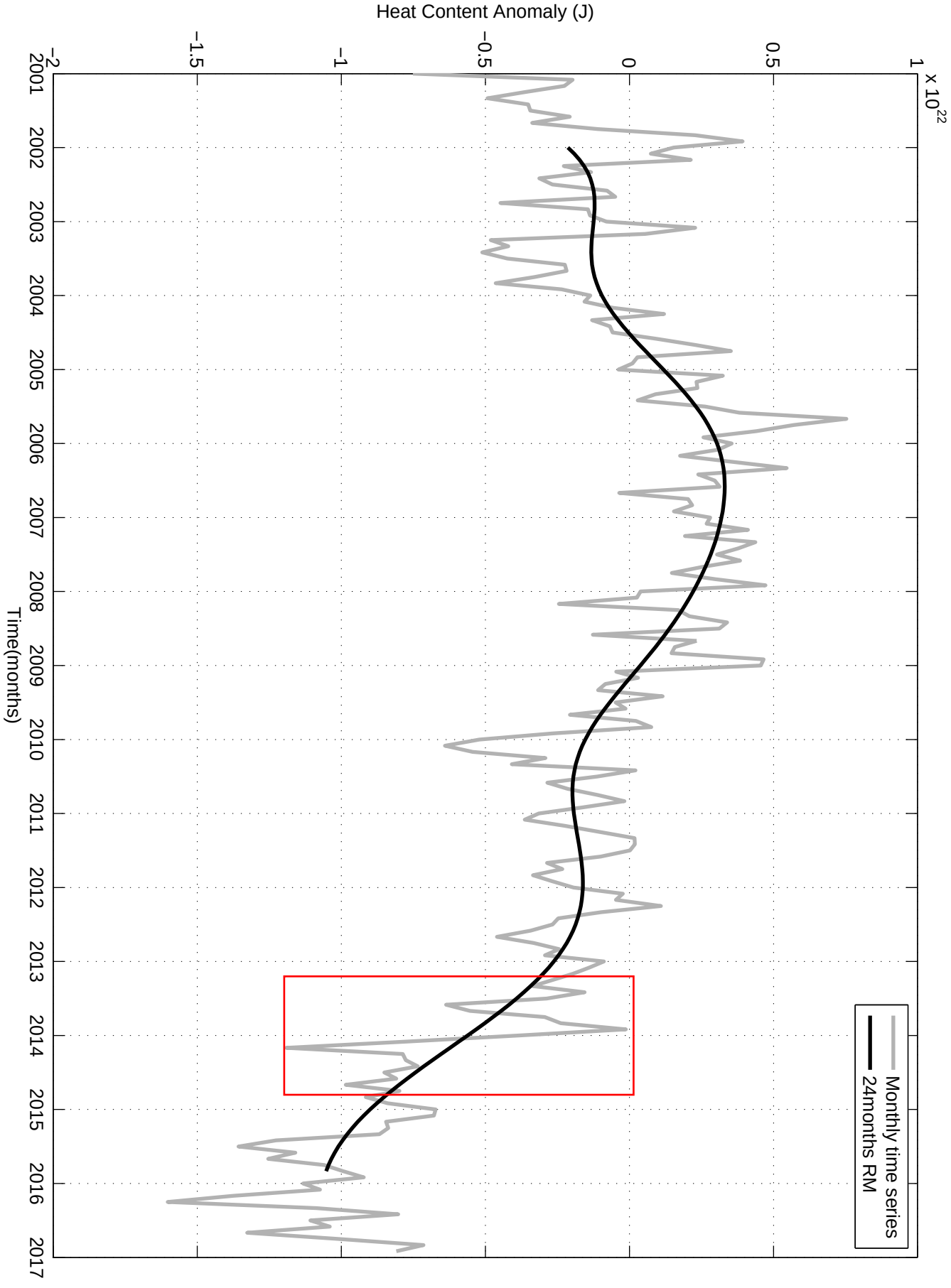
Heat Content Anomaly (J)
x 10^22
1
0.5
0
−0.5
−1
−1.5
−2
2001
2002
2003
2004
2005
2006
2007
2008
2009
2010
2011
2012
2013
2014
2015
2016
2017
Time(months)
Monthly time series
24months RM

Fig. 10

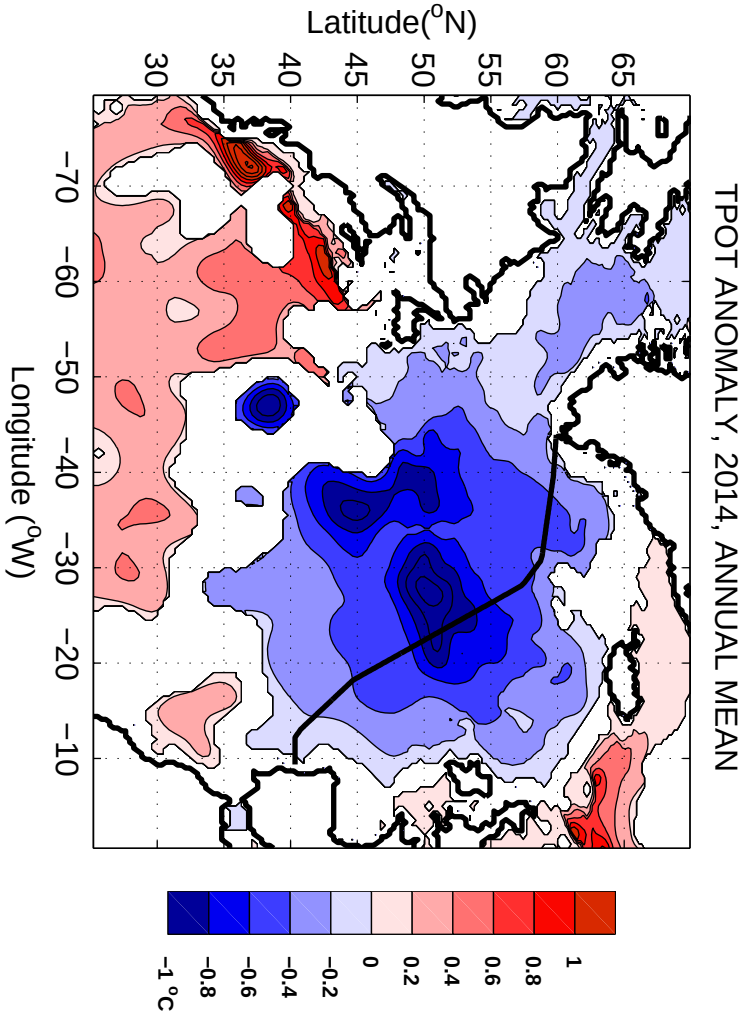
TPOT ANOMALY, 2014, ANNUAL MEAN
Latitude(°N)
30
35
40
45
50
55
60
65
Longitude (°W)
−70
−60
−50
−40
−30
−20
−10
−1 °C
−0.8
−0.6
−0.4
−0.2
0
0.2
0.4
0.6
0.8
1

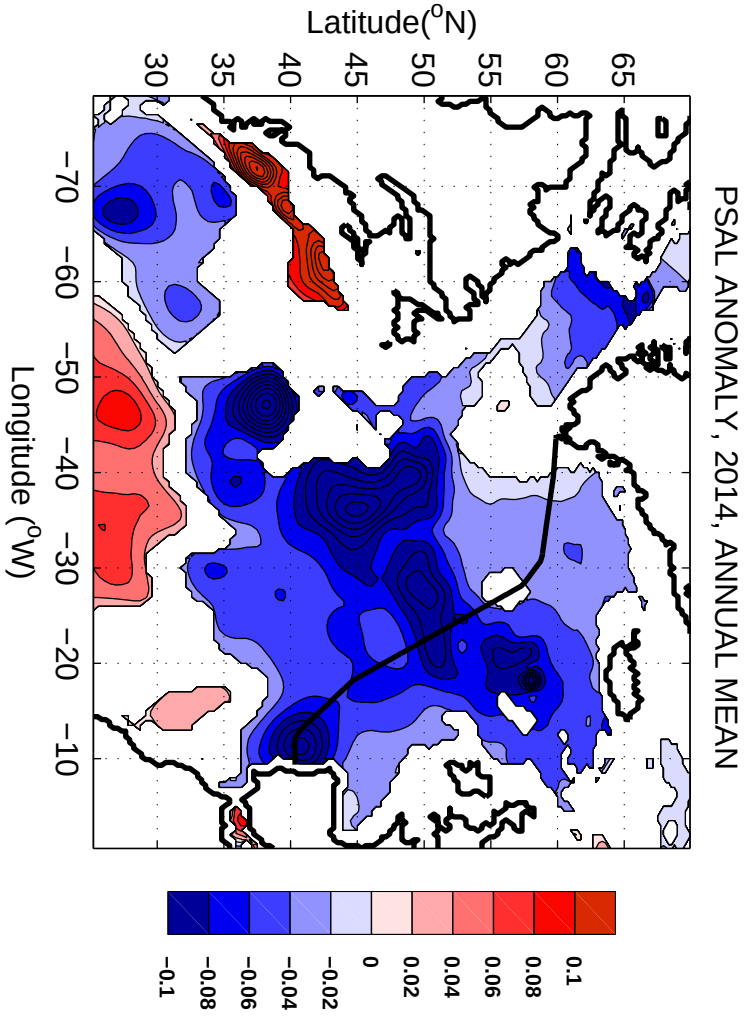
PSAL ANOMALY, 2014, ANNUAL MEAN
Latitude(°N)
30
35
40
45
50
55
60
65
Longitude (°W)
−70
−60
−50
−40
−30
−20
−10
−0.1
−0.08
−0.06
−0.04
−0.02
0
0.02
0.04
0.06
0.08
0.1

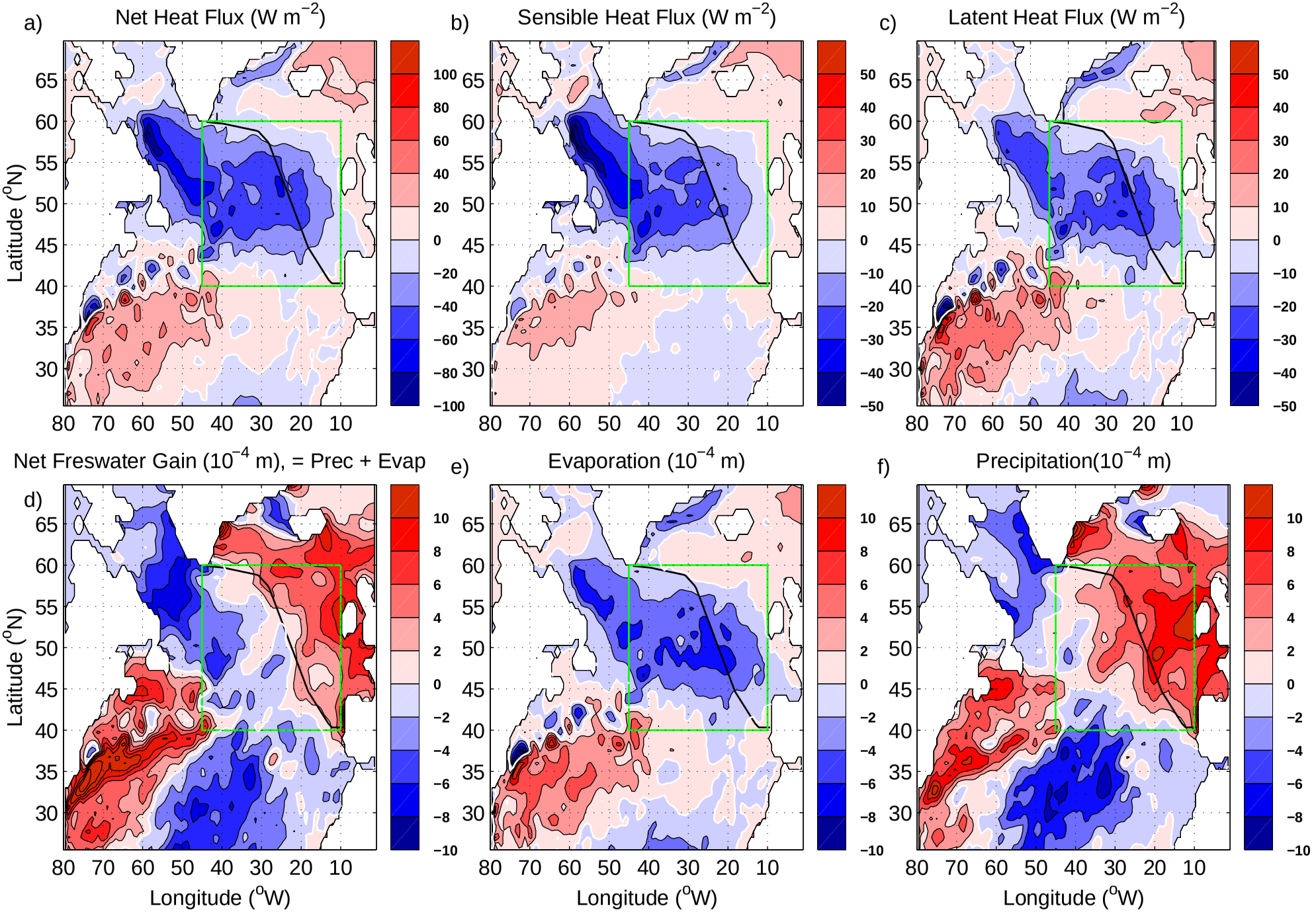
a)
Net Heat Flux (W m^{-2})
b)
Sensible Heat Flux (W m^{-2})
c)
Latent Heat Flux (W m^{-2})
d)
Net Freswater Gain (10^{-4} m), = Prec + Evap
e)
Evaporation (10^{-4} m)
f)
Precipitation(10^{-4} m)
Latitude (^{o}N)
Longitude (^{o}W)
80 70 60 50 40 30 20 10
30 35 40 45 50 55 60 65
100 80 60 40 20 0 −20 −40 −60 −80 −100
50 40 30 20 10 0 −10 −20 −30 −40 −50
10 8 6 4 2 0 −2 −4 −6 −8 −10

Fig. 11

Fig. 12

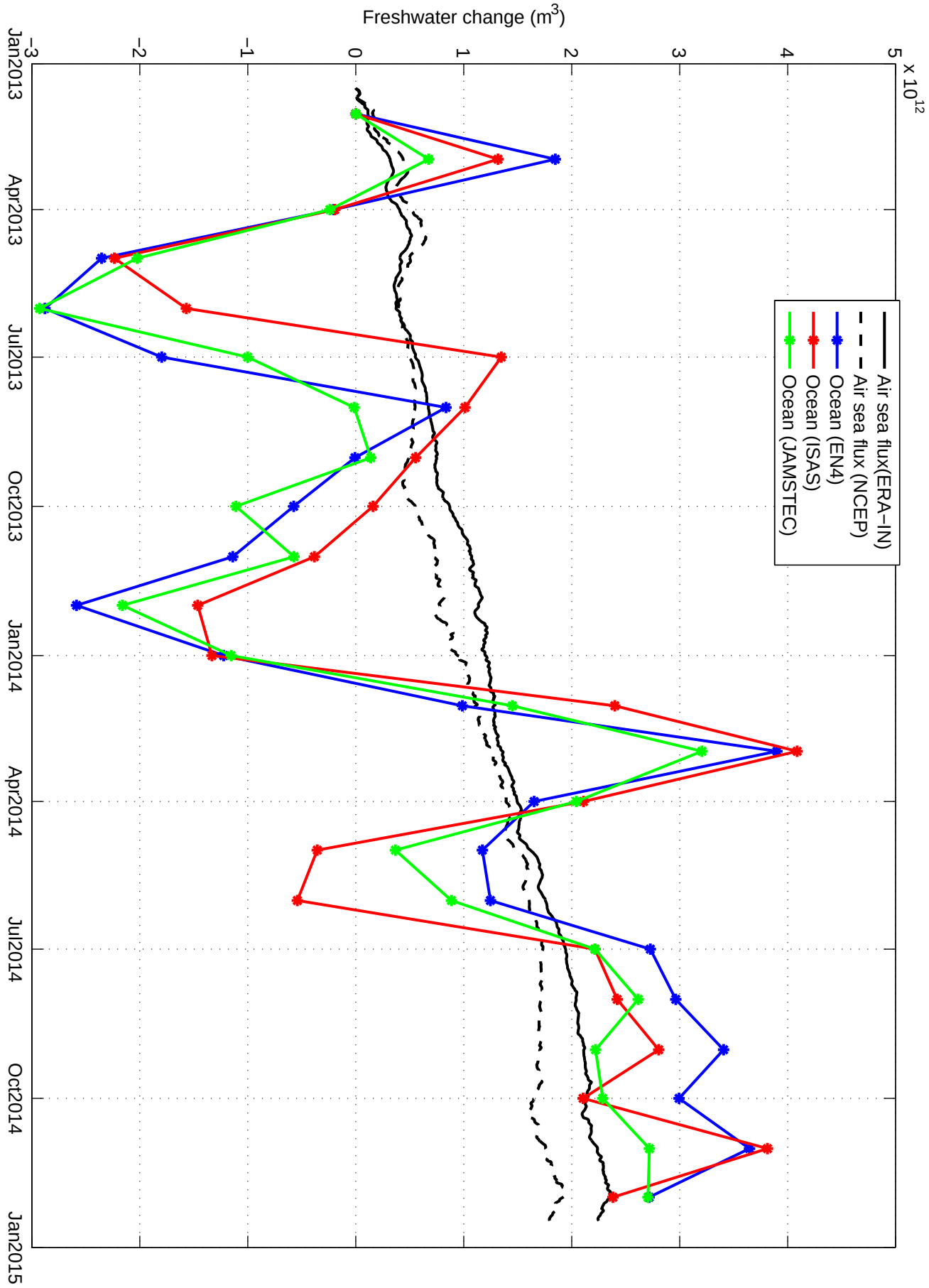
Freshwater change (m3)
x 10^12
5
4
3
2
1
0
−1
−2
−3
Jan2013
Apr2013
Jul2013
Oct2013
Jan2014
Apr2014
Jul2014
Oct2014
Jan2015
Air sea flux(ERA−IN)
Air sea flux (NCEP)
Ocean (EN4)
Ocean (ISAS)
Ocean (JAMSTEC)